
1 Remote-sensing algorithm for surface evapotranspiration

2 considering landscape and statistical effects on mixed-pixels

3 ZhiQing Peng ^{a,b}, Xiaozhou Xin ^{a,*}, JinJun Jiao ^{a,b}, Ti Zhou ^{a,b}, Qinhuo Liu ^{a,c}

4 *a. State Key Laboratory of Remote Sensing Science, Institute of Remote Sensing and Digital Earth*

5 *Chinese Academy of Sciences, Beijing 100101, China*

6 *b. University of Chinese Academy of Sciences, Beijing 100049, China*

7 *c. Joint Center for Global Change Studies (JCGCS), Beijing 100875, China*

8 Abstract

9 Evapotranspiration (ET) plays an important role in surface-atmosphere interactions and can be
10 monitored using remote sensing data. However, surface heterogeneity, including the inhomogeneity
11 of landscapes and surface variables, significantly affects the accuracy of ET estimated from satellite
12 data. The objective of this study is to assess and reduce the uncertainties resulting from surface
13 heterogeneity in remotely sensed ET using Chinese HJ-1B satellite data, which is of 30 m spatial
14 resolution in VIS/NIR bands and 300 m spatial resolution in the TIR band. A temperature sharpening
15 and flux aggregation scheme (TSFA) was developed to obtain accurate heat fluxes from the HJ-1B
16 satellite data. The IPUS (input parameter upscaling) and TRFA (temperature resampling and flux
17 aggregation) methods were used to compare with the TSFA in this study. The three methods repre-
18 sent three typical schemes used to handle mixed pixels from the simplest to the most complex. IPUS
19 handles all surface variables at coarse resolution of 300 m in this study, TSFA handles them at 30 m
20 resolution, and TRFA handles them at 30m and 300m resolution, which depends on the actual spatial
21 resolution. Analyzing and comparing the three methods can help us to get a better understanding of
22 spatial scale errors in remote sensing of surface heat fluxes. *In situ* data collected during HiWATER-
23 MUSOEXE (Multi-Scale Observation Experiment on Evapotranspiration over heterogeneous land
24 surfaces of The Heihe Watershed Allied Telemetry Experimental Research) were used to validate
25 and analyze the methods. ET estimated by TSFA exhibited the best agreement with *in situ* observa-
26 tions, and the footprint validation results showed that the R^2 , MBE, and RMSE values of the sensible
27 heat flux (H) were 0.61, $0.90 \text{ W}\cdot\text{m}^{-2}$ and $50.99 \text{ W}\cdot\text{m}^{-2}$, respectively, and those for the latent heat flux
28 (LE) were 0.82, $-20.54 \text{ W}\cdot\text{m}^{-2}$ and $71.24 \text{ W}\cdot\text{m}^{-2}$, respectively. IPUS yielded the largest errors in ET
29 estimation. The RMSE of LE between the TSFA and IPUS methods was $51.30 \text{ W}\cdot\text{m}^{-2}$, and the
30 RMSE of LE between the TSFA and TRFA methods was $16.48 \text{ W}\cdot\text{m}^{-2}$. Furthermore, additional
31 analysis showed that the TSFA method can capture the sub-pixel variations of land surface temper-
32 ature and the influences of various landscapes within mixed pixels.

33 **Index Terms:** surface heterogeneity, temperature sharpening, area weighting, energy balance, evapo-
34 transpiration, spatial scale, HJ-1B satellite

35 1. Introduction

36 Five types of methods have been developed to estimate evapotranspiration (ET) or latent heat
37 flux (LE) via remote sensing. (1) Surface energy balance models calculate LE as a residual term.
38 According to the partitioning of the sources and sinks of the Soil-Plant-Atmosphere Continuum
39 (SPAC), surface energy balance models can be classified as one-source (Bastiaanssen et al., 1998;

1 Su, 2002; Allen et al., 2007; Long and Singh, 2012a) or two-source models (Shuttleworth and Wal-
2 lace, 1985; Norman et al., 1995; Xin and Liu, 2010; Zhu et al., 2013). (2) Penman-Monteith models
3 are used to calculate LE by using the Penman-Monteith equation and numerous surface resistance
4 parameterization schemes that control the diffusion of evaporation from soil surfaces and transpira-
5 tion from plant canopies. These two-source Penman-Monteith models separate soil evaporation
6 from plant transpiration (Cleugh et al., 2007; Mu et al., 2011; Leuning et al., 2008; Chen et al., 2013;
7 Sun et al., 2013; Mallick et al., 2015). (3) Land surface temperature-vegetation index (LST-VI) space
8 methods assign the dry and wet edges of the LST-VI feature space as minimum and maximum ET,
9 respectively. These methods interpolate the media, and use the Penman-Monteith or Priestley-Taylor
10 equation to calculate the LE (Jiang and Islam, 1999, 2001; Sun et al., 2011; Long and Singh, 2012b;
11 Yang and Shang, 2013; Fan et al., 2015; Zhang et al., 2005). (4) Priestley-Taylor models expand the
12 range of the Priestley-Taylor coefficient in the Priestley-Taylor equation (Jiang and Islam, 2003; Jin
13 et al., 2011) or combine the physiological force factors with the energy component of ET (Fisher et
14 al., 2008; Yao et al., 2013). (5) Additional methods include empirical/statistical methods (Wang and
15 Liang, 2008; Yebra et al., 2013) and the use of complementary based models (Venturini et al., 2008)
16 and land-process models with data assimilation schemes (Bateni and Liang, 2012; Xu et al., 2015).

17 If the operational algorithm can be described as a linear combination of inputs, or if the surface
18 variables and landscapes are homogeneous at the pixel scale, scale error does not exist (Hu and
19 Islam, 1997). However, it is difficult to develop linear operational models due to the complexity of
20 mass and heat transfer processes between the atmosphere and land surface. ET estimation models
21 have been generally developed for simple and homogeneous surface conditions. However, hetero-
22 geneity is a natural attribute of the surface of the Earth. Therefore, larger spatial scale errors occur
23 when these remotely sensed models are applied to calculate the regional ET using satellite data.

24 In previous studies, researchers have coupled high- and low-resolution satellite data and statis-
25 tically quantified the inhomogeneity of mixed pixels to correct the scale error in ET estimations
26 using (1) temperature downscaling, which converts images from a lower (coarser) to higher (finer)
27 spatial resolution using statistical-based models with regression or stochastic relationships among
28 parameters (Kustas et al., 2003; Norman et al., 2003; Cammalleri et al., 2013; Ha et al., 2013), (2)
29 the correction-factor method, which uses sub-pixel landscapes information to determine the correc-
30 tion factor of scale bias (Maayar and Chen, 2006) and (3) the area-weighting method, which calcu-
31 lates roughness length and sensible heat flux based on sub-pixel landscapes (Xin et al., 2012). These
32 correction methods mainly focus on two problems: inhomogeneity of landscapes and inhomogene-
33 ity of surface variables.

34 Studies have shown that different landscapes (Blyth and Harding, 1995; Moran et al., 1997;
35 Bonan et al., 2002; McCabe and Wood, 2006) and the sub-pixel variations of surface variables, such
36 as stomatal conductance (Bin and Roni, 1994), or leaf area index (Bonan et al., 1993; Maayar and
37 Chen, 2006), can cause errors in turbulent heat flux estimations. Surface variables inhomogeneity
38 is rather difficult to evaluate, as the sub-pixel variation of surface variables can be large, even in the
39 pure pixels. For example, generally, temperatures over land surfaces vary strongly in space and time,
40 and it is common for the LST to vary by more than 10 K over just a few centimeters of distance or
41 by more than 1 K in less than a minute over certain cover types (Li et al., 2013b). However, in case
42 of mixed pixels, surface variables such as land surface temperature are commonly considered as
43 single value to represent the entire pixel area in ET estimation models, which results in large errors.

44 The focus of this study is on the effects of surface heterogeneity when estimating ET. Based

1 on the satellite products that are currently available, three methods were used to analyze the uncer-
2 tainties produced by surface heterogeneity: (1) input parameter upscaling (IPUS) does not consider
3 the surface heterogeneities at all. It was designed to simulate the satellites that have identical spatial
4 resolutions both the visible near-infrared (VNIR) and thermal infrared (TIR) bands; (2) temperature
5 resampling and flux aggregation (TRFA) does not consider the heterogeneity of LST; and (3) tem-
6 perature sharpening and flux aggregation (TSFA) considers all the surface heterogeneities. These
7 methods were designed for use with the majority of satellite data or products that have inconsistent
8 spatial resolutions between the VNIR and TIR bands, such as the Landsat and HJ-1B satellites.

9 The surface variables in this paper were mainly derived from HJ-1B satellite data. The Chinese
10 HJ-1A/B satellites were launched on September 6, 2008, and were designed for disaster and envi-
11 ronmental monitoring, as well as other applications. The HJ-1B satellites are equipped with two
12 charge-coupled device (CCD) cameras and one infrared scanner (IRS) with spatial resolutions of 30
13 m and 300 m, respectively. Compared to high-temporal-resolution satellite data, such as the MODIS
14 satellite data, or high-spatial resolution satellite data, such as the Landsat 7 or 8 satellites data, HJ-
15 1B data has the advantage of a high spatiotemporal resolution. Since the satellites were launched,
16 the HJ-1/CCD time series data have been widely used in China to accurately classify land cover
17 (Zhong et al., 2014a) and monitor various environmental disasters (Wang et al., 2010). Land-based
18 variables, such as leaf area index (LAI), land surface temperature (LST), and downward longwave
19 radiation (L_d), have been retrieved by the HJ-1 satellites using algorithms developed by Chen et al.
20 (2010), Li et al. (2010a, 2011a) and Yu et al. (2013), respectively. These variables lay the foundation
21 for ET research.

22 Although the HJ-1B satellites provide CCD data with a high spatial resolution of 30 m, the
23 spatial resolution of the thermal infrared (TIR) band is only 300 m. Thus, surface heterogeneity
24 effects must be considered when estimating the heat flux.

25 **2. Methodology**

26 **2.1. Temperature-sharpening method based on statistical relationships**

27 Surface thermal dynamics affect ET. The spatial resolution of TIR images is usually not as high
28 as the spatial resolution of visible near-infrared (VNIR) bands because the energy of VNIR photons
29 is higher than the energy of thermal photons. Thus, the inhomogeneity of TIR images would be
30 larger than the inhomogeneity of VNIR images. Since the land surface temperature is calculated
31 from the TIR band, the uncertainty of the variables becomes unpredictable when the inhomogeneity
32 of TIR images is enhanced. Therefore, land surface temperature data should be derived with a high
33 spatial resolution.

34 The land surface temperature can be reconstructed at the spatial resolution of the VNIR images
35 by using a statistical temperature-sharpening strategy proposed by Kustas et al. (2003). This method
36 assumes that the negative correlation between the Normalized Difference Vegetation Index (NDVI)
37 and LST is invariant. The NDVI reflects vegetation growth and coverage, and the LST reflects sur-
38 face thermal dynamics. The LST decreases with increasing vegetation cover. The scatter plot be-
39 tween the LST and NDVI values forms a feature space that is applicable at different scales when
40 sufficient number of pixels exist.

41 HJ-1B satellite images can provide vegetation and thermal information at spatial resolutions of
42 30 m and 300 m, respectively. The 300 m resolution thermal data cannot sufficiently distinguish the

1 surface temperatures of small targets within pixels. However, this issue can be addressed by tem-
 2 perature sharpening based on the functional relationship between NDVI and LST. A flowchart of
 3 temperature sharpening is shown in Fig. 1, and LST at the NDVI pixel resolution can be derived
 4 based on the following steps (Kustas et al., 2003):

5 (1) The $NDVI_{30}$ is aggregated to 300 m NDVI ($NDVI_{300}$). Then, the $NDVI_{300}$ is divided into
 6 three classes ($0 \leq NDVI_{300} < 0.2$, $0.2 \leq NDVI_{300} < 0.5$ and $0.5 \leq NDVI_{300}$).

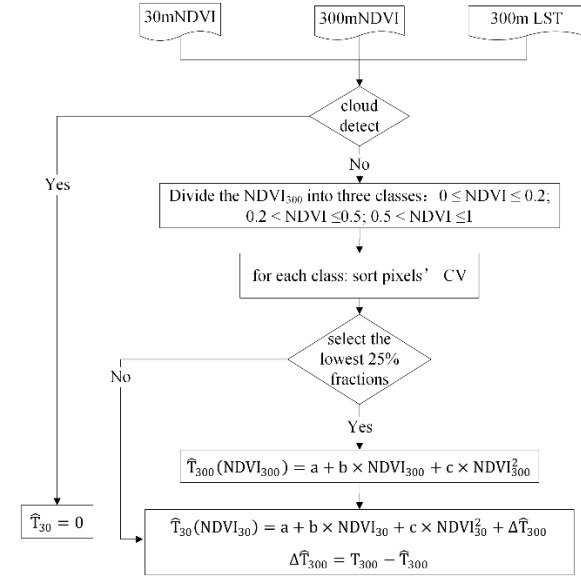
7 (2) A subset of pixels is selected from the scene where the NDVI is as homogeneous as possible
 8 at a pixel resolution of 300 m based on the coefficient of variation (CV). The CVs are calculated
 9 using the original 30 m NDVI data ($NDVI_{30}$) as follows:

$$10 \quad CV = \frac{STD}{mean} \quad (1)$$

11 where STD and mean are the standard deviation and the average values of 10×10 pixels of $NDVI_{30}$,
 12 respectively. The CVs are sorted from smallest to largest. Lower CVs corresponds to more homo-
 13 geneous land surface values, and a threshold should be determined to guarantee that a sufficient
 14 number of pixels is available for least squares fitting between $NDVI_{300}$ and T_{300} . Therefore, the
 15 fractions of 25% of the lowest CVs are selected from each class.

16 (3) A least squares expression is established between $NDVI_{300}$ and T_{300} using the selected
 17 pixels.

$$18 \quad \hat{T}_{300}(NDVI_{300}) = a + b \times NDVI_{300} + c \times NDVI_{300}^2 \quad (2)$$



19
 20 **Figure 1.** Flowchart of temperature sharpening.

21 (4) For each 30 m pixel within a 300 m pixel, \hat{T}_{30} can be calculated according to Eq. (2) as
 22 follows:

$$23 \quad \hat{T}_{30}(NDVI_{30}) = a + b \times NDVI_{30} + c \times NDVI_{30}^2 + \Delta \hat{T}_{300} \quad (3)$$

24 where $\Delta \hat{T}_{300} = T_{300} - \hat{T}_{300}$ is the deviation between the regressed temperature and the tempera-
 25 ture that was observed by the satellite at 300 m.

26 **2.2. Area-weighting method based on landscape information**

27 Coarse pixels are inhomogeneous because various types of land use may be included. Using a
 28 dominant type to represent such a large landscape is irrational. The spatial resolution of LST is
 29 significantly increased by temperature sharpening in section 2.1. Consequently, all inputs of ET

1 algorithms can be obtained at high spatial resolutions. Then, inhomogeneity issues can be greatly
 2 diminished by dividing the landscape into finer pixels.

3 Combined with a high-resolution classification map, sub-pixel scale parameters can be used in
 4 the ET algorithm, which is more rational than using a dominant class type because different land-
 5 scapes may require different ET algorithms. The surface energy fluxes can be averaged linearly due
 6 to the conservation of energy (Kustas et al., 2003), and a simple average that calculates the arithme-
 7 tic mean over sub-pixels is the best choice for flux upscaling (Ershadi et al., 2013b). Thus, the
 8 aggregated flux at a low resolution $F(x, y)$ is the arithmetic mean of all the $n \times n$ sub-pixel fluxes
 9 that constitute the contributing flux $F(x_i, y_j)$ at coordinate (x_i, y_j) :

$$10 \quad F(x, y) = \frac{1}{n \times n} \sum_{i=1}^n \sum_{j=1}^n F(x_i, y_j) \quad (4)$$

11 Because the average of the sub-pixels fluxes is equal to the area-weighted sum of each land-
 12 type result, the final coarse result can be derived from the area-weighted sum of each land type
 13 result within the landscape. The main steps in the area-weighting process are shown below (Xin et
 14 al., 2012):

15 (1) Geometric correction and registration of the VNIR and TIR input datasets.

16 (2) Count the area ratios of different land cover types within each pixel of a low-spatial-reso-
 17 lution classification image.

18 (3) According to the fine-classification data, different parameterization schemes can be used in
 19 the ET algorithm to calculate the sub-pixel flux, such as the net radiation (R_n), soil heat flux (G) and
 20 sensible heat flux (H).

21 (4) To calculate the regional flux, the flux of the large pixel is calculated by the area-weighting
 22 method as follows:

$$23 \quad F = \sum_{i=1}^n w_i \cdot F_i \quad (5)$$

24 where w_i is the fractional area contributing flux F_i of class type i and F is the aggregated flux
 25 at the coarse resolution. The LE is computed as a residual of the surface energy balance in the TSFA
 26 (see section 2.3) process, in which a high-spatial resolution image is used to reduce the number of
 27 mixed pixels.

28 **2.3. Pixel ET algorithm**

29 The surface energy balance describes the energy between the land surface and atmosphere. The
 30 energy budget is commonly expressed as follows:

$$31 \quad R_n = LE + H + G \quad (6)$$

32 where R_n is the net radiation, G is the soil heat flux, H is the sensible heat flux, and LE is the
 33 latent heat flux absorbed by water vapor when it evaporates from the soil surface and transpires
 34 from plants through stomata. The widely used one-source energy balance model considers a homo-
 35 geneous SPAC medium and ignores the inhomogeneity and structure. In this case, LE can be ex-
 36 pressed as follows:

$$37 \quad LE = \frac{\rho c_p}{\gamma} \cdot \frac{e_s - e_a}{r_a + r_s} \quad (7)$$

38 where γ is the psychrometric constant; e_s and e_a are the aerodynamic saturation vapor pressure
 39 and atmospheric water vapor pressure, respectively; and r_a and r_s are the water vapor transfer
 40 aerodynamic resistance and surface resistance, respectively. Surface resistance includes soil re-

1 sistance and canopy resistance. The surface resistance is influenced by the physiological character-
 2 istics of the vegetation and the water supply of roots. Thus, it is difficult to obtain surface resistance
 3 via remote sensing, and surface resistance is highly uncertain, particularly over heterogeneous sur-
 4 faces. To avoid error introduced by the uncertainty of the surface resistance, LE is computed as a
 5 residual of the surface energy balance equation.

6 R_n is the difference between incoming and outgoing radiation and is calculated as follows:

$$7 \quad R_n = S_d(1 - \alpha) + \varepsilon_s L_d - \varepsilon_s \sigma T_{rad}^4 \quad (8)$$

8 where S_d is the downward shortwave radiation, α is the surface broadband albedo, ε_s is the
 9 emissivity of the land surface, L_d is the downward atmospheric longwave radiation, $\sigma = 5.67 \times$
 10 $10^{-8} \text{W} \cdot \text{m}^{-2} \cdot \text{K}^{-4}$ is the Stefan-Boltzmann constant and T_{rad} is the surface radiation tempera-
 11 ture.

12 G is commonly estimated using the empirical relationship with R_n . Because the canopy exerts
 13 a significant influence on G , the fractional canopy coverage FVC is used to determine the ratio of
 14 G to R_n as follows:

$$15 \quad G = R_n \times [\Gamma_c + (1 - \text{FVC}) \times (\Gamma_s - \Gamma_c)] \quad (9)$$

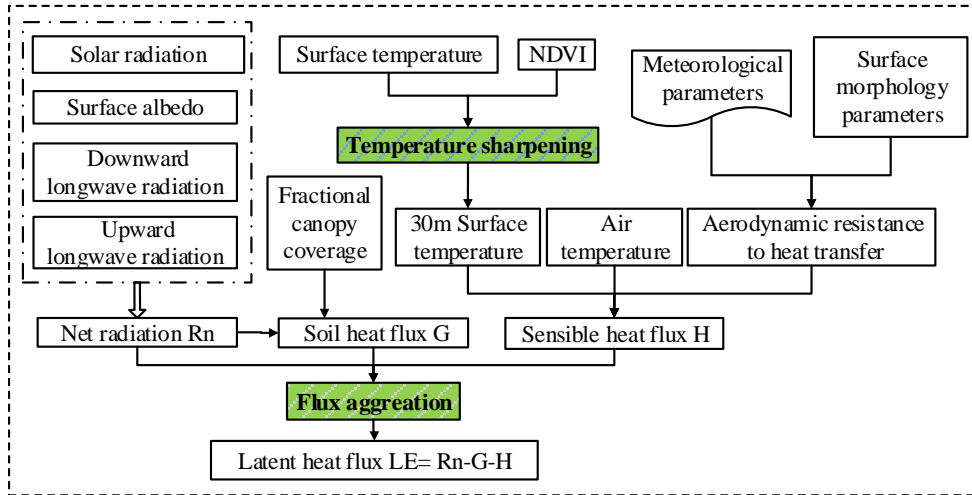
16 where Γ_s is 0.315 for bare soil and Γ_c is 0.05 for a full vegetation canopy (Su, 2002). H is the
 17 transfer of turbulent heat between the surface and atmosphere, which is driven by a temperature
 18 difference and controlled by resistances that depend on local atmospheric conditions and land cover
 19 properties (Kalma et al., 2008). According to gradient diffusion theory, the equation for H is as
 20 follows:

$$21 \quad H = \rho c_p \frac{T_{aero} - T_a}{r_a} \quad (10)$$

22 where ρ is the density of the air; c_p is the specific heat of the air at a constant pressure; T_{aero} is
 23 the aerodynamic surface temperature obtained by extrapolating the logarithmic air temperature pro-
 24 file to the roughness length for heat transport; T_a is the air temperature at a reference height; and
 25 r_a is the aerodynamic resistance, which influences the heat transfer between the source of the tur-
 26 bulent heat flux and the reference height. Aerodynamic resistance was calculated based on the
 27 Monin-Obukhov similarity theory (MOST) using a stability correction function (Paulson, 1970;
 28 Ambast et al., 2002). The zero-plane displacement height, d , and roughness length, z_{om} , were pa-
 29 rameterized by the schemes proposed by Choudhury and Monteith (1988).

30 In this approach, H must be accurately estimated. However, calculating H using Eq. (10) is
 31 difficult. Because remote sensing cannot obtain T_{aero} , the value of T_{aero} is generally replaced with
 32 the radiative surface temperature T_{rad} , which is not always equal to T_{aero} . The difference between
 33 these terms for homogeneous and full-coverage vegetation is approximately 1-2°C (Choudhury et
 34 al., 1986), and it can reach 10°C in sparsely vegetative areas (Kustas, 1990). The method that cor-
 35 rects for this discrepancy adds “excess” resistance r_{ex} to r_a . We used the brief method proposed
 36 by Chen (1988) to calculate r_{ex} : $r_{ex} = 4/u_*$.

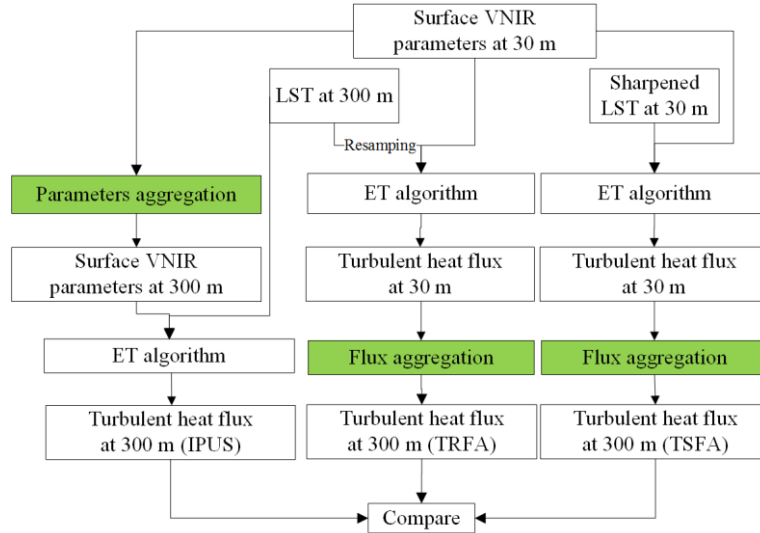
37 Fig. 2 shows the flowchart for merging ET retrieval and temperature sharpening based on HJ-
 38 1B satellites.



1
2
3
4
5
6
7
8
9
10
11
12
13

Figure 2. Flowchart of ET retrieval using the “Temperature Sharpening and Flux Aggregation” method.

The spatial scale effect is generally revealed by a discrepancy between different upscaling methods. In one method, parameters are upscaled to a large scale before calculating the heat flux. In the other method, heat flux is calculated at a small scale, and the results are then upscaled. In this study, the resolution of the final output result is 300 m. To evaluate the heterogeneity reducing effect of TSFA, two other upscaling methods called IPUS and TRFA were implemented (see Fig. 3). In the case of IPUS, the inputs of the energy balance model are first retrieved at 30 m resolution (see section 3.2.1.1) and then aggregated to 300 m resolution. Subsequently, these 300 m inputs are used in the one-source energy balance model to obtain the four energy balance components at 300 m resolution. In TRFA, the LST at 300 m is first resampled to 30 m using the nearest neighbour method and the 30 m resolution inputs are used for estimating ET. The outputs of the four energy-balance components of the TRFA are obtained using the area-weighting method shown in section 2.2.



14
15

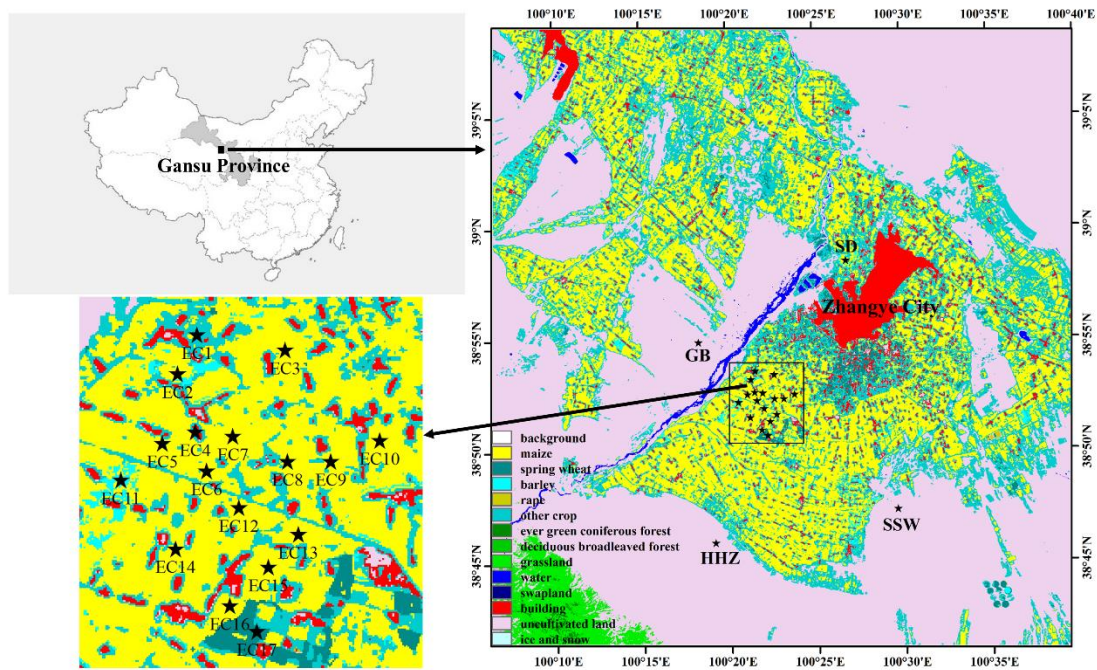
Figure 3. Flowchart of the three upscaling methods for retrieving evapotranspiration

16 3. Study area and Dataset

17 3.1. Study area

18 Our study was conducted in the middle stream of the Heihe River Basin (HRB), which is lo-
19 cated near the city of Zhangye in the arid region of Gansu Province in northwestern China

1 (100.11 E-100.16 E, 39.10 N-39.15 N). The middle reach of the HRB is a typical desert-oasis ag-
 2 riculture ecosystem dominated by maize and wheat. Areas of the Gobi Desert and the alpine vege-
 3 tation in the Qilian Mountains are located near the study area (see Fig. 4). The artificial oasis is
 4 highly heterogeneous, which impacts the thermal-dynamics and hydraulic features. Consequently,
 5 the water use efficiency and ET are variable. The Heihe River Basin has long served as a test bed
 6 for integrated watershed studies, as well as land surface and hydrological experiments. Comprehen-
 7 sive experiments, such as the Watershed Allied Telemetry Experimental Research (WATER) project
 8 (Li et al., 2009), and an international experiment - the Heihe Basin Field Experiment (HEIFE) as
 9 part of the World Climate Research Programme (WCRP), have been conducted in this basin. One
 10 major objective of HiWATER was to capture the strong land surface heterogeneities and associated
 11 uncertainties within a watershed (Li et al., 2013a).



12
 13 **Figure 4.** Study area and distribution of EC towers in HiWATER-MUSOEXE

14 **3.2. Dataset**

15 In this study, data are mainly derived from the HJ-1B satellite. We combined these data with
 16 ancillary data and *in situ* “Multi-Scale Observation Experiment on Evapotranspiration over hetero-
 17 geneous land surfaces of The Heihe Watershed Allied Telemetry Experimental Research” (Hi-
 18 WATER-MUSOEXE) data to estimate and validate the HJ-B land surface variables and heat fluxes.

19 **3.2.1. Remote sensing data**

20 **3.2.1.1. HJ-1B satellite data**

21 The specifications of HJ-1B are shown in Table 1. The satellite has quasi-sun-synchronous
 22 orbits at an altitude of 650 km, a swath width of 700 km and a revisit period of 4 days. Combined,
 23 the revisit period of the satellites is 48 h. Because HJ-1 CCDs lack an onboard calibration system,
 24 cross-calibration methods were proposed to calibrate the CCD instruments (Zhang et al., 2013;
 25 Zhong et al., 2014b). The image quality of the HJ-1A/B CCD is stable, the performances of each

band are balanced (Zhang et al., 2013) and the radiometric performance of the HJ-1A/B CCD sensors is similar to the performances of the Landsat-5 TM, Observer-1 (EO-1) Advanced Land Imager and Terra ASTER. The image quality of the HJ-1 CCD is very similar to the image quality of Landsat-5 TM (Jiang et al., 2013). In addition, the accuracy of the TIR band's onboard calibration meets the land surface temperature retrieval requirements but not the sea surface temperature retrieval requirements (Li et al., 2011b). The Center for Resources Satellite Data and Application (CRESDA) in China releases calibration coefficients annually on its website (<http://www.cresda.com>). These data are freely available from the CRESDA website (<http://218.247.138.121/DSSPlatform/index.html>).

Table 1. Specifications of the HJ-1B main payloads

Sensor	Band	Spectral range (μm)	Spatial resolution (m)	Swath width (km)	Revisit time (days)
CCD	1	0.43-0.52	30	360 (single)	4
	2	0.52-0.60			
	3	0.63-0.69		700 (two)	
	4	0.76-0.90			
IRS	5	0.75-1.10	150	720	4
	6	1.55-1.75			
	7	3.50-3.90	300		
	8	10.5-12.5			

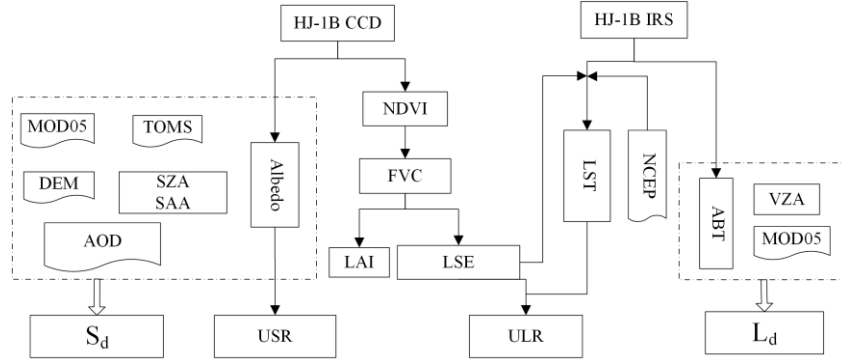


Figure 5. Flowchart of land surface variable retrieval. The abbreviations are defined as follows: SZA: solar zenith angle; SAA: solar azimuth angle; VZA: view zenith angle; AOD: aerosol optical depth; ABT: at-nadir brightness temperature; S_d : downward shortwave radiation; USR: upward shortwave radiation, ULR: upward longwave radiation; and L_d : downward longwave radiation.

We used the HJ-1B satellite data from the HRB region in 2012. Because many variable-retrieving algorithms require clear-sky conditions when calculating ET, we combined data quality information with visual interpretation to select satellite images without clouds. Considering the period of ground observations discussed in section 3.2.2, we obtained data for 11 days: June 19, June 30, July 8, July 27, August 2, August 15, August 22, August 29, September 2, September 13 and September 14.

The HJ-1B satellite data of the HRB were pre-processed, including geometric correction, radiometric calibration, and atmospheric correction. The following surface variables are needed in Eqs. (1) to (10): downward shortwave radiation, downward longwave radiation, emissivity, albedo, fractional vegetation coverage (FVC), cloud mask data, meteorological data, LAI and LST. Fig. 5 illustrates a flowchart of the retrieval of these variables.

(1) Surface albedo. According to the algorithm proposed by Liang et al. (2005) and Liu et al. (2011a), surface albedo was obtained from the top of the atmosphere (TOA) reflectance by the HJ-

1 satellite using a lookup table based on an angular bin regression relationship. The surface albedo and bidirectional reflectance distribution function (BRDF) of the HJ-1 satellite in the regression procedure were monitored using POLDER-3/PARASOL BRDF datasets, and BRDF was used to obtain the TOA reflectance in the 6S (Second Simulation of a Satellite Signal in the Solar Spectrum) radiation transfer mode.

2 (2) NDVI, FVC and LAI. The NDVI is the regression kernel of the temperature-sharpening procedure and is used to calculate the FVC. Atmospherically corrected surface reflectance values were used to calculate the NDVI as follows:

$$9 \quad \text{NDVI} = \frac{\rho_{\text{nir}} - \rho_{\text{red}}}{\rho_{\text{nir}} + \rho_{\text{red}}} \quad (11)$$

10 and

$$11 \quad \text{FVC} = \frac{\text{NDVI} - \text{NDVI}_s}{\text{NDVI}_v + \text{NDVI}_s} \quad (12)$$

12 where ρ_{nir} and ρ_{red} are the reflectances in the near-infrared and red band, respectively, and NDVI_v and NDVI_s are the fully vegetated and bare soil NDVI values, respectively. As an important input for the parameterization of surface roughness length and aerodynamic resistance, the LAI was determined using the following equation (Nilson, 1971):

$$13 \quad P(\theta) = e^{-G(\theta) \cdot \Omega \cdot \text{LAI} / \cos(\theta)} \quad (13)$$

$$14 \quad P(\theta) = 1 - \text{FVC} \quad (14)$$

15 where θ is the zenith angle, $P(\theta)$ is the angular distribution of the canopy gap fraction, $G(\theta)$ is the projection coefficient (0.5) and Ω is the total foliage clumping index, which can be obtained from the GLC global clumping index database according to the land use type (He et al., 2012).

16 (3) Land surface emissivity (LSE). LSE is needed to calculate the R_n and is extremely important for retrieving LST. In this paper, LSE was calculated using the FVC as follows (Valor and Caselles, 1996):

$$17 \quad \varepsilon = \varepsilon_v \cdot \text{FVC} + \varepsilon_g(1 - \text{FVC}) + 4 \langle d\varepsilon \rangle \cdot \text{FVC} \cdot (1 - \text{FVC}) \quad (15)$$

18 where ε is the LSE, $\langle d\varepsilon \rangle$ is an effective value of the cavity effect of emissivity, the mean $d\varepsilon$ of all vegetation species in this study is $\langle d\varepsilon \rangle = 0.015$, ε_v and ε_g are the vegetation and ground emissivity, respectively.

19 (4) Land surface temperature. A single-channel parametric model for retrieving LST based on HJ-1B/IRS TIR data developed by Li et al. (2010a) was employed to obtain the LST. This model was developed from a parametric model based on MODTRAN4 using NCEP atmospheric profile data.

20 (5) Downward shortwave radiation. In this study, the algorithm proposed by Li et al. (2010b) was applied. MOD05, TOMS, aerosol and solar angle data were used to estimate the direct light flux and diffuse light flux using a lookup table that was generated via the 6S radiation transfer mode (Vermote et al., 2006). This method considered the influences of complex terrain, and a topographic correction was performed by using products of the ASTER digital elevation model (DEM).

21 (6) Downward longwave radiation (L_d). The TOA brightness temperature of the HJ-1B thermal channel was used to substitute the atmospheric effective temperature. Effective atmospheric emissivity was parameterized as an empirical function of the water vapor content. These values were substituted for atmospheric temperature and atmospheric emissivity to estimate the value of L_d . Because this L_d retrieval method proposed by Yu et al. (2013) was only valid for clear-sky conditions,

cloud masking information was used to determine clear skies. When cloud contamination existed in the image, the brightness temperature was relatively low, causing the L_d to be lower than that in the cloudless images.

3.2.1.2. Ancillary data

Ancillary data were used because the bands of the satellite could not invert all of the variables needed to retrieve ET.

(1) Atmospheric water vapor data. MODIS provides water vapor data (MOD05), including a 1-km near-infrared product and a 5-km thermal-infrared product, every day. The 1-km near-infrared water vapor product was used to retrieve L_d in this study.

(2) Surface elevation data. We used the 30 m resolution Global Digital Elevation Model (GDEM) based on ASTER, which covers 83°N–83°S, to derive S_d .

(3) Atmosphere ozone data. A Total Ozone Mapping Spectrometer (TOMS), which was carried on an Earth Probe (EP) satellite, was used to derive S_d . The TOMS-EP provided daily global atmospheric ozone data at a resolution of 1°×1.25° (Li et al., 2010b).

(4) Atmosphere profile data. Global reanalysis data from the National Centers for Environmental Prediction (NCEP) were used to derive LST. These data were generated globally every 6 hours (0:00, 06:00, 12:00, 18:00 UTC) for every 1° of latitude and longitude (Li et al., 2010a).

3.2.2. HiWATER experiment dataset

The *in situ* HRB observation data were provided by HiWATER. From June to September 2012, HiWATER designed nested observation matrices over 30 km×30 km and 5.5 km×5.5 km within the middle stream oasis in Zhangye to focus on the heterogeneity of the scale effect in HiWATER-MUSOEXE.

In the larger observation matrix, four eddy covariance (EC) systems and one superstation were installed in the oasis–desert ecosystem. Each station was supplemented with an automatic meteorological station (AMS) to record meteorological and soil variables and monitor the spatial–temporal variations of ET and its associated factors (Li et al., 2013a). The station information is shown in Table 2, and the distribution of the stations is shown in Fig. 4. Within the artificial oasis, an observation matrix composed of 17 EC towers and ordinary AMSs exists where the superstation was located. The land surface was heterogeneous and dominated by maize, maize inter-cropped with spring wheat, vegetables, orchards and residential areas (Li et al., 2013a). Because the EC16 and HHZ stations lacked R_n and G observation data, they were excluded from this study.

Table 2. The *in situ* HiWATER-MUSOEXE station information

Station	Longitude (°)	Latitude (°)	Tower height (m)	Altitude (m)	Land cover
EC1	100.36E	38.89N	3.8	1552.75	vegetation
EC2	100.35E	38.89N	3.7	1559.09	maize
EC3	100.38E	38.89N	3.8	1543.05	maize
EC4	100.36E	38.88N	4.2	1561.87	building
EC5	100.35E	38.88N	3	1567.65	maize
EC6	100.36E	38.87N	4.6	1562.97	maize
EC7	100.37E	38.88N	3.8	1556.39	maize
EC8	100.38E	38.87N	3.2	1550.06	maize

EC9	100.39E	38.87N	3.9	1543.34	maize
EC10	100.40E	38.88N	4.8	1534.73	maize
EC11	100.34E	38.87N	3.5	1575.65	maize
EC12	100.37E	38.87N	3.5	1559.25	maize
EC13	100.38E	38.86N	5	1550.73	maize
EC14	100.35E	38.86N	4.6	1570.23	maize
EC15	100.37E	38.86N	4.5	1556.06	maize
EC17	100.37E	38.85N	7	1559.63	orchard
GB	100.30E	38.91N	4.6	1562	uncultivated land-Gobi
SSW	100.49E	38.79N	4.6	1594	uncultivated land-desert
SD	100.45E	38.98N	5.2	1460	swamp land

1 The ground observation data included the H and LE. Reliable methods were used to ensure the
2 quality of the turbulent heat flux data. Before the main campaign, an intercomparison of all instru-
3 ments was conducted in the Gobi Desert (Xu et al., 2013). After basic processing, including spike
4 removal and corrections for density fluctuations (WPL correction), a four-step procedure was per-
5 formed to control the quality of the EC data. In this procedure, data were rejected when (1) the
6 sensor was malfunctioned, (2) precipitation occurred within 1 h before or after collection, (3) the
7 ratio of missing data was greater than 3% in the 30 min raw record and (4) the friction velocity was
8 below 0.1 ms^{-1} at night (for more details see Liu et al., 2011b; Xu et al., 2013; Liu et al., 2016). EC
9 outputs are available every 30 min. G was measured by using three soil heat plates at a depth of 6
10 cm at each site, and the surface G was calculated using the method proposed by Yang and
11 Wang(2008) based on the soil temperature and moisture above the plates. Surface meteorological
12 variables, such as wind speed, wind direction, relative humidity and air pressure, were used to in-
13 terpolate images using the inverse distance weighting. Researchers can obtain these data from the
14 websites of the Cold and Arid Regions Science Data Center at Lanzhou (<http://card.westgis.ac.cn/>)
15 or the Heihe Plan Data Management Center (<http://www.heihedata.org/>).

16 Energy imbalances are common in ground flux observations. The conserving Bowen ratio
17 (H/LE) and residual closure technique are often used to force the energy balance. Computing the
18 LE as a residual variable may be a better method for energy balance closure under conditions with
19 large LEs (small or negative Bowen ratios due to strong advection) (Kustas et al., 2012). Thus, the
20 residual closure method was applied because the “oasis effect” was distinctly observed in the desert-
21 oasis system on clear days during the summer (Liu et al., 2011b).

22 4. Results and analysis

23 4.1. Evaluation of surface variables

24 To control model inputs and analyse error sources, the coarse-resolution land surface temper-
25 ature, downward shortwave radiation, downward longwave radiation, R_n and G were evaluated
26 using *in situ* data.

27 The ground-based land surface temperature, T_s , was calculated using the Stefan-Boltzman
28 Law from the AMS measurements of the longwave radiation fluxes (Li et al., 2014) as follows:

$$29 \quad T_s = \left[\frac{L^\uparrow - (1 - \epsilon_s) \cdot L^\downarrow}{\epsilon_s \cdot \sigma} \right]^{\frac{1}{4}} \quad (16)$$

30 in which L^\uparrow and L^\downarrow are *in situ* surface upwelling and atmospheric downwelling longwave radiation,

1 respectively, and ε_s is the surface broadband emissivity, which is regarded as the pixel value of the
 2 HJ-1B at the AMS. The coefficient of determination R^2 , mean bias error (MBE) and root mean
 3 square error (RMSE) of the LST are 0.71, -0.14 K and 3.37 K, respectively. As shown in Table 3,
 4 the accuracy of EC4 is low. The main causes of the large errors are as follows: (1) buildings and
 5 soil/vegetation are distinct materials, the LSE algorithm may not be suitable for buildings and (2)
 6 the EC4 foundation is non-uniform and is not suitable for validation. After removing the EC4 data,
 7 the R^2 , MBE and RMSE values of the LSTs were 0.83, 0.69 K and 2.51 K, respectively. The LST
 8 errors of SSW and SD were large due to large errors on particular days. For example, although it
 9 was briefly cloudy above station SSW on July 27, this area was not identified as cloudy in the cloud
 10 detection process.

11

Table 3. The station validation results of land surface temperature

Station	R^2	MBE (K)	RMSE (K)	Station	R^2	MBE (K)	RMSE (K)
EC1	0.82	0.18	1.74	EC11	0.42	1.59	2.98
EC2	0.82	0.59	1.54	EC12	0.87	0.62	1.51
EC3	0.69	0.38	1.90	EC13	0.83	0.44	1.48
EC4	0.83	-9.87	10.04	EC14	0.73	1.43	2.44
EC5	0.83	1.71	2.34	EC15	0.74	1.53	2.41
EC6	0.61	0.30	2.44	EC17	0.78	1.20	2.32
EC7	0.82	0.39	1.40	GB	0.69	0.12	2.33
EC8	0.83	0.45	1.55	SSW	0.59	1.38	3.82
EC9	0.63	2.31	3.15	SD	0.76	-3.83	4.84
EC10	0.68	1.32	2.45				

12

13

14

15

16

17

The R^2 , MBE and RMSE values of S_d were 0.81, 13.80 $W \cdot m^{-2}$, and 25.35 $W \cdot m^{-2}$, respectively. The station validation results are shown in Table 4. The accuracy of SSW is low. Because cloudy conditions occurred briefly on July 27, few ground observations were obtained, and S_d was significantly overestimated. After removing these data, the R^2 , MBE and RMSE values of S_d at SSW were 0.87, 10.90 $W \cdot m^{-2}$ and 21.13 $W \cdot m^{-2}$, respectively.

Table 4. The station validation results of downward shortwave radiation

Station	R^2	MBE ($W \cdot m^{-2}$)	RMSE ($W \cdot m^{-2}$)	Station	R^2	MBE ($W \cdot m^{-2}$)	RMSE ($W \cdot m^{-2}$)
EC1	0.97	25.23	27.73	EC11	0.90	30.11	33.76
EC2	0.84	28.29	33.57	EC12	0.96	24.35	26.43
EC3	0.97	17.56	19.25	EC13	0.93	12.41	17.92
EC4	0.98	6.07	9.34	EC14	0.98	32.40	33.49
EC5	0.98	10.60	12.29	EC15	0.94	26.71	29.71
EC6	0.93	27.68	30.71	EC17	0.94	-20.25	24.54
EC7	0.89	-17.69	27.59	GB	0.89	25.34	30.63
EC8	0.83	15.63	25.50	SSW	0.63	18.51	34.93
EC9	0.96	-2.27	9.96	SD	0.98	5.70	13.82
EC10	0.94	-3.50	11.97				

18

19

The R^2 , MBE and RMSE values of the HRB L_d were 0.73, 0.28 $W \cdot m^{-2}$, and 21.24 $W \cdot m^{-2}$, respectively. As seen in Table 5, the accuracies at EC3, SD and SSW were low. The low accuracies

at EC3 and SD potentially resulted from (1) high humidity, which resulted in low at-nadir brightness temperatures and low retrieved L_d , or (2) instrument error, which occurred because the EC3 ground observations were always greater than those of the other stations during the same period. Although SSW was located in a desert, the ground-air temperature difference was large. The L_d retrieval may have a large error because the models use surface temperature when estimating L_d to approximate or substitute the near-surface temperature (Yu et al., 2013). The corrected error of our L_d retrieving algorithm resulted from the ground-air temperature difference in non-vegetated areas. The inaccuracy of the SSW LST may influence the L_d results.

Table 5. The station validation results of downward longwave radiation

Station	R ²	MBE (W·m ⁻²)	RMSE (W·m ⁻²)	Station	R ²	MBE (W·m ⁻²)	RMSE (W·m ⁻²)
EC1	0.85	4.16	17.21	EC11	0.93	-2.72	10.55
EC2	0.88	0.11	14.23	EC12	0.87	-0.84	14.80
EC3	0.91	-35.65	37.88	EC13	0.86	-7.28	15.98
EC4	0.88	3.36	16.38	EC14	0.82	4.07	16.42
EC5	0.88	-0.79	15.02	EC15	0.85	17.67	23.06
EC6	0.84	2.55	15.43	EC17	0.90	-1.11	12.87
EC7	0.75	-5.90	19.72	GB	0.88	9.50	27.82
EC8	0.80	-1.35	17.49	SSW	0.85	25.33	34.50
EC9	0.86	10.44	17.99	SD	0.85	-26.54	34.08
EC10	0.87	7.98	16.05				

The R², MBE and RMSE values of the HRB R_n were 0.70, -9.64 W·m⁻², and 42.77 W·m⁻², respectively. The station-validated results of R_n are shown in Table 6, which indicates that the accuracies of EC4, EC7, EC17 and SSW were relatively low. According to the sensitivity analysis of Eq. (8), L_d and S_d are highly sensitive variables when calculating R_n , while the albedo, LSE and LST are not as sensitive. Although LST was not a sensitive variable, the MBE and RMSE values of LST at EC4 reached -9.87 K and 10.04 K because the land cover of EC4 was maize at 300 m resolution. However, the observation tower was located in a built-up area, which potentially caused errors when estimating R_n . The accuracies of S_d and L_d at EC7 were low on several days, and MBE=-43.40 W·m⁻² and RMSE=50.50 W·m⁻² after removing these data. EC17 was located in an orchard, and the signal that was received by the sensors at EC17 was affected by the complex vertical structure of the orchard ecosystem. The information of substrate plants may be ignored, leading to albedo retrieval errors. An albedo bias of 0.03 can lead to an R_n error of approximately 20 W·m⁻² when the solar incoming radiation is large. As previously discussed, it was briefly cloudy on July 27, and after removing those data, the R², MBE and RMSE values of the R_n obtained at station SSW were 0.72, 8.20 W·m⁻², and 37.60 W·m⁻², respectively.

Table 6. The station net radiation validation results

Station	R ²	MBE (W·m ⁻²)	RMSE (W·m ⁻²)	Station	R ²	MBE (W·m ⁻²)	RMSE (W·m ⁻²)
EC1	0.76	-2.55	30.61	EC11	0.86	-15.13	28.05
EC2	0.79	2.52	25.24	EC12	0.90	-8.46	19.38
EC3	0.86	-35.84	42.97	EC13	0.88	-25.73	32.34
EC4	0.84	76.64	80.25	EC14	0.90	4.23	18.18

EC5	0.85	-24.41	32.34	EC15	0.84	8.33	23.01
EC6	0.82	4.35	23.44	EC17	0.89	-62.62	68.11
EC7	0.61	-58.66	67.83	GB	0.77	-10.40	38.86
EC8	0.83	-20.62	32.45	SSW	0.44	23.05	62.93
EC9	0.87	-29.60	36.27	SD	0.75	19.98	35.24
EC10	0.83	-24.35	33.51				

The R^2 , MBE and RMSE values of the G in the HRB were 0.57, 8.51 $W \cdot m^{-2}$, and 29.73 $W \cdot m^{-2}$, respectively. The station-validated G results are shown in Table 7. At EC5, the soil temperature and moisture were the same at different depths after July 19, which resulted in a surface G that was equal to the G at a depth of 6 cm. G below the surface was usually less than the G at the soil surface; thus, the validation results of G at EC5 indicate that G was overestimated. At SSW, the brief cloudy period decreased the observed soil surface temperature, which decreased the calculated surface G. However, the remotely sensed G did not reflect this situation. In this case, the G was overestimated because the R_n was overestimated. After removing the data on July 27, the R^2 , MBE and RMSE values of the G at SSW were 0.17, 19.34 $W \cdot m^{-2}$, and 33.30 $W \cdot m^{-2}$, respectively.

Table 7. The station validation results of the soil heat flux

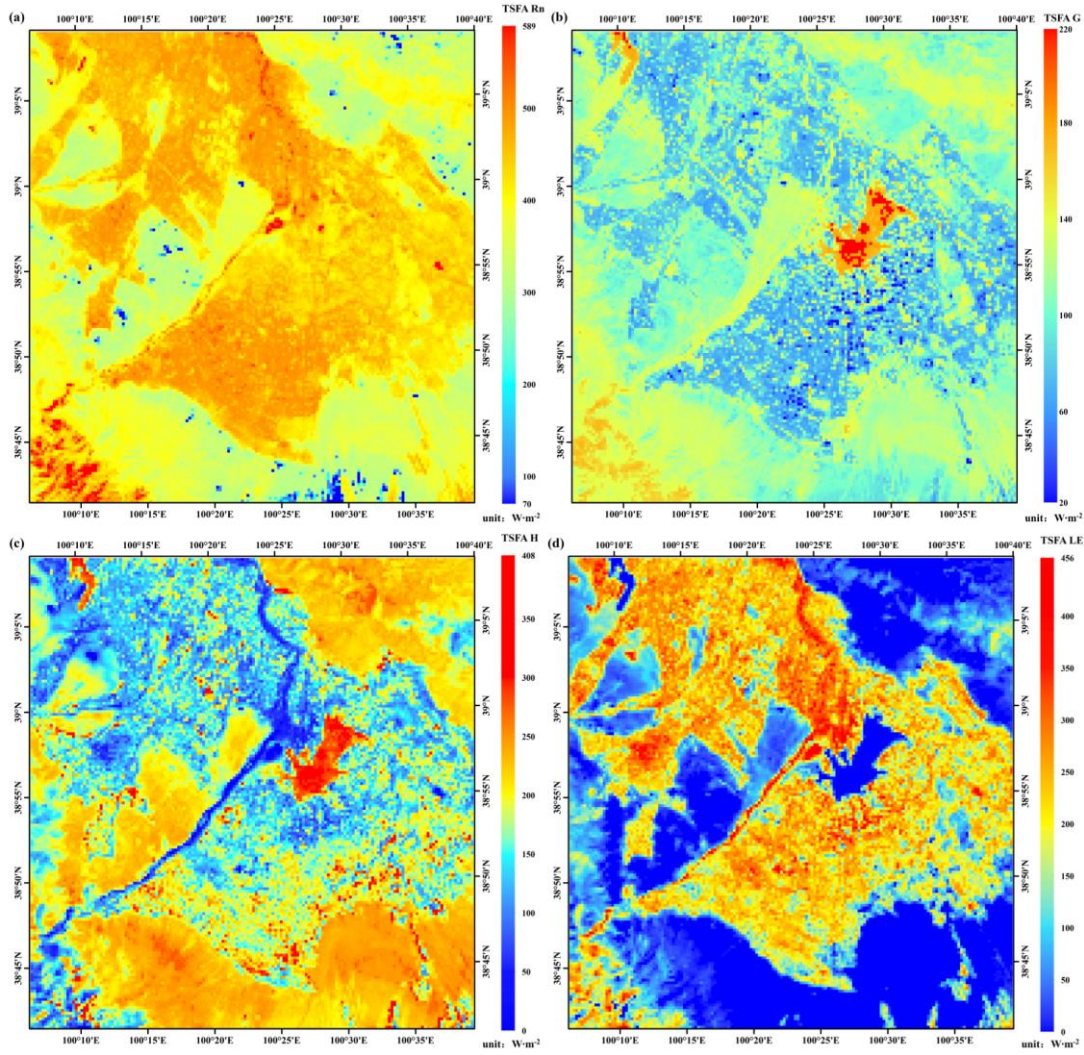
tation	R^2	MBE ($W \cdot m^{-2}$)	RMSE ($W \cdot m^{-2}$)	Station	R^2	MBE ($W \cdot m^{-2}$)	RMSE ($W \cdot m^{-2}$)
EC1	0.50	19.73	31.53	EC11	0.71	4.23	19.23
EC2	0.24	20.78	28.72	EC12	0.53	20.29	24.79
EC3	0.03	-1.15	36.28	EC13	0.91	-0.89	17.27
EC4	0.45	18.50	22.29	EC14	0.82	-1.89	18.72
EC5	0.38	41.87	60.19	EC15	0.78	6.68	15.80
EC6	0.83	-5.91	14.57	EC17	0.49	8.26	33.59
EC7	0.28	7.50	24.65	GB	0.29	-17.86	26.81
EC8	0.68	-5.73	20.15	SSW	0.01	30.41	51.87
EC9	0.61	6.83	26.96	SD	0.71	-4.79	13.71
EC10	0.41	7.68	28.67				

4.2. Validation of heat fluxes by TSFA

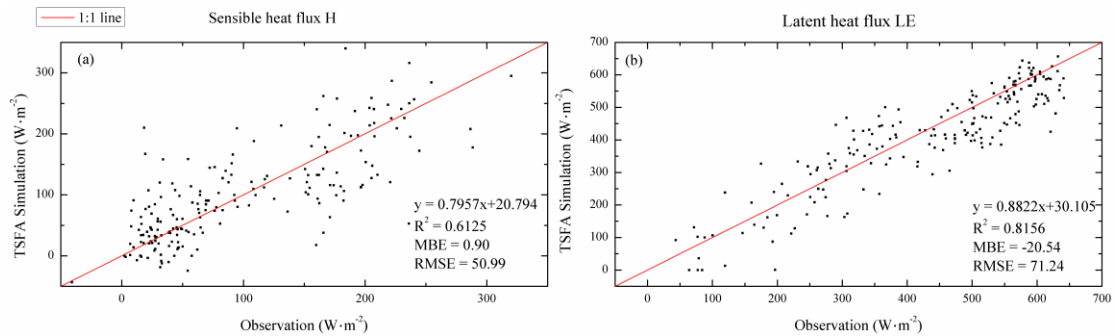
Fig. 6 provides the turbulent heat flux results calculated by TSFA on September 13, 2012. The spatial distribution of the turbulent heat flux is obvious. The H values of buildings and uncultivated land, including land patches in the Gobi region, barren areas and desert areas, were high, in addition to the LEs of water and agricultural areas in the oasis. The southern areas of the images show uncultivated barren land bordering the Qilian Mountains that resulted from snowmelt and the downward movement of water. In these areas, the groundwater levels are high and the soil moisture content is approximately 30% based on *in situ* measurements at a depth of 2 cm. Therefore, the LE values of barren areas in the south are higher than the LE values of desert areas in the southeast, although both areas were classified as uncultivated land.

Studies have shown that validation methods that consider the source area are more appropriate for evaluating ET models than traditional validation methods based on a single pixel (Jia et al., 2012; Song et al., 2012). In this study, a user-friendly tool presented by Neftel et al. (2008), which is based on the Eulerian analytic flux footprint model proposed by Kormann and Meixner (2001) was used

1 to calculate the footprints of the function parameters. The continuous footprint function was dis-
 2 persed based on the relative weights of the pixels in which the source area was located.



3
 4 **Figure 6.** Maps of the four energy components, (a) Rn, (b) G, (c) H and (d) LE, calculated by TSFA on September
 5 13, 2012.



6
 7 **Figure 7.** Scatter plot of the TSFA turbulent heat flux results

8 The footprint validation results of the TSFA turbulent heat fluxes are shown in Fig. 7 and Table
 9 8. The R^2 , MBE and RMSE of H were 0.61, 0.90 $W \cdot m^{-2}$ and 50.99 $W \cdot m^{-2}$, respectively, and those
 10 of LE were 0.82, -20.54 $W \cdot m^{-2}$ and 71.24 $W \cdot m^{-2}$, respectively. Because LE was calculated as a
 11 residual term, it was impacted by R_n , surface G and H. The errors of all inputs may contribute to

the LE, which complicates the error sources of the LE. These errors are discussed in detail in sections 4.3.2 and 4.4.

Table 8. *In situ* validation results of heat flux using the TSFA

Date	TSFA-H($W \cdot m^{-2}$)			TSFA-LE($W \cdot m^{-2}$)		
	R ²	MBE	RMSE	R ²	MBE	RMSE
0619	0.39	44.73	66.38	0.69	-44.15	80.60
0630	0.73	23.71	38.96	0.88	-63.81	77.83
0708	0.55	32.70	58.72	0.85	-43.02	72.32
0727	0.90	-34.34	43.59	0.92	26.74	57.60
0803	0.80	-4.77	18.92	0.78	-4.58	47.86
0815	0.74	-18.37	38.82	0.93	4.75	35.41
0822	0.40	31.64	66.21	0.65	-44.44	93.81
0829	0.79	23.01	38.36	0.79	-50.45	77.99
0902	0.21	-45.10	74.81	0.54	24.39	69.31
0913	0.25	-9.64	41.01	0.59	-59.36	82.77
0914	0.31	-34.11	50.88	0.47	27.99	67.50

As shown in Fig. 7, the majority of the H values are small because June, July, August and September constitute the growing season when ET greatly cools the air. The temperature difference between the land surface and air is small, leading to a low H. The points with large H values are influenced by uncultivated land. In our study area, Gobi region, barren area and desert area comprise the uncultivated land. The points in the scatter plot with large H values represent desert, where the H values reach approximately $300 W \cdot m^{-2}$. Some points in the H scatter plot are less than 0 due to inversion from the “oasis effect” or irrigation. For example, the HiWATER soil moisture data show that irrigation occurred on August 22, 2012. Irrigation is the main source of water within the oasis and cools the land surface to temperatures below the air temperature. In addition, irrigation leads to errors in LST retrieval because it increases the atmospheric water vapor content, as discussed in section 4.1. The model error is further analyzed in section 4.4.

4.3. Comparison between TSFA, TRFA and IPUS

To verify whether the TSFA method can simulate the heterogeneity of the land surface, the TRFA and IPUS methods were also implemented for comparison purposes. These three methods were evaluated using (1) validation of TRFA and IPUS based on *in situ* measurements and (2) quantitative analysis based on the spatial distribution and scatter plots of the four energy balance components.

4.3.1. Validation of the TRFA and IPUS heat fluxes

Table 9 provides the *in situ* validation results of H and LE calculated using the IPUS and TRFA methods. Compared to validation results of TSFA in Table 8, the TSFA produced a better retrieval accuracy than the TRFA, and the TRFA was better than the IPUS on all days and the MBE and RMSE values of TSFA decreased and the R² of TSFA increased on most days. Table 9 shows that the improvements in accuracy between TRFA and IPUS were relatively larger than those between TSFA and TRFA. Compared to the IPUS results, the TRFA results were similar to the TSFA results because sub-pixel landscapes and sub-pixel variations of most variables were considered. Thus, TRFA effectively decreased the scale error that resulted from heterogeneity because the 30 m VNIR

1 data were fully used. However, the performance of the TRFA method is unstable. For example, on
 2 August 3 and August 29, the TRFA results were slightly worse than the IPUS results. This situation
 3 occurred because the different sub-pixel landscape temperatures were considered as equal to the
 4 values estimated at the 300 m resolution. Thus, when values of LST at 300 m scale have large
 5 retrieval errors, the turbulent heat flux retrieval error may be amplified by the sub-pixel landscapes.

6 **Table 9.** *In situ* validation results of the turbulent heat fluxes of IPUS and TRFA

date	IPUS-H($W \cdot m^{-2}$)			IPUS-LE ($W \cdot m^{-2}$)			TRFA-H ($W \cdot m^{-2}$)			TRFA-LE ($W \cdot m^{-2}$)		
	R ²	MBE	RMSE	R ²	MBE	RMSE	R ²	MBE	RMSE	R ²	MBE	RMSE
0619	0.32	48.53	71.70	0.66	-47.68	86.02	0.39	52.28	70.98	0.65	-46.71	85.93
0630	0.50	41.45	67.30	0.80	-81.75	102.33	0.69	42.64	60.85	0.86	-78.50	93.98
0708	0.34	44.17	77.45	0.63	-66.75	118.63	0.44	54.20	76.00	0.82	-63.82	89.11
0727	0.81	-33.14	50.01	0.83	25.61	74.26	0.84	-23.53	41.76	0.86	14.82	65.21
0803	0.84	-5.23	33.50	0.74	-3.98	60.49	0.80	7.76	37.51	0.76	-18.23	62.71
0815	0.64	-23.28	47.89	0.85	10.32	54.98	0.70	-14.77	39.99	0.89	0.59	45.22
0822	0.31	41.50	74.81	0.61	-53.60	102.12	0.40	40.63	69.94	0.65	-54.17	98.97
0829	0.72	27.15	44.16	0.76	-54.76	83.20	0.75	30.79	44.97	0.77	-59.43	86.22
0902	0.28	-52.44	83.25	0.51	32.89	76.48	0.21	-45.77	75.84	0.52	24.37	71.69
0913	0.08	-11.45	57.50	0.61	-57.38	81.83	0.06	-11.89	49.63	0.54	-57.78	84.58
0914	0.12	-36.52	67.38	0.28	19.46	89.30	0.03	-34.34	64.85	0.38	25.41	75.96

7 Variations in landscape characteristics systematically trigger variations in surface variables.
 8 Landscape inhomogeneity can be classified using two conditions: nonlinear vegetation density vari-
 9 ations between sub-pixels (e.g., different types of vegetation mixed with each other or with bare
 10 soil) and coarse pixels containing different landscapes (e.g., vegetation or bare soil mixed with
 11 buildings or water). To evaluate the effects of TSFA, stations with a typical severe heterogeneous
 12 surface at EC4, a weak heterogeneous surface at EC11, a typical pixel (called “TP” hereafter) at the
 13 boundary of the oasis and bare soil (sample 62, line 102 in the image of study area), and a uniform
 14 surface at EC15, were selected to analyze the temperature sharpening results.

15 EC4 is used as an example because its land cover and sub-pixel variations of temperature were
 16 complicated. Table 10 compares the turbulent heat fluxes calculated using the IPUS, TRFA and
 17 TSFA methods. Significant differences were observed between the TSFA and IPUS results and be-
 18 tween the TRFA and IPUS results due to the heterogeneity of the surface. The LE calculated using
 19 the TSFA method was more consistent with *in situ* measurements than the LE calculated using the
 20 IPUS method because the MBE and RMSE decreased considerably, the R² increased, and the accu-
 21 racy was improved by approximately $40 W \cdot m^{-2}$. However, the LE calculated by the TRFA was more
 22 accurate than the LE calculated by the TSFA, as discussed below.

23 The H calculated by using the TSFA method was more accurate than the H calculated by using
 24 the TRFA and IPUS methods. The RMSE of the results from the TRFA method was relatively close
 25 to the RMSE of the results from the TSFA method because the TRFA method also considers the
 26 effects of the heterogeneity of landscapes. In addition, the H values obtained from the TRFA method
 27 were always greater than those obtained from the TSFA method. Because the TSFA turbulent heat
 28 flux results are the same as the TRFA turbulent heat flux results for buildings and water bodies in
 29 our pixel ET algorithm, the differences between the TSFA and TRFA results depend on the vegeta-
 30 tion and bare soil. Additionally, the 300 m resolution LST is larger than the LST of the sub-pixels,
 31 such as pixels containing vegetation or bare soil. This relationship occurs for two reasons: (1) the

coarse pixels contain buildings and result in a larger 300 m resolution LST and (2) the LSTs were underestimated at EC4 (as shown in Table 3), which would underestimate the value of $\Delta\hat{T}_{300}$ in Eq. (3) and, consequently, the sharpening temperature at 30 m and H. Because the LE was calculated as a residual item in the energy balance equation, the errors of the other three energy balance components accumulate in the LE term. At EC4, the R_n was overestimated by approximately $80 \text{ W}\cdot\text{m}^{-2}$, as discussed in section 4.1, but the scale effect of R_n was not obvious (see section 4.3.2), and the G was overestimated by approximately $20 \text{ W}\cdot\text{m}^{-2}$. These results decreased the accuracy of the available energy and overestimated the error by $60 \text{ W}\cdot\text{m}^{-2}$. Because the TRFA overestimates H, the underestimation of H in the TSFA would result in larger overestimation of LE than that estimated by the TRFA. Consequently, the LE calculated by using the TSFA method is less accurate than the LE calculated by the TRFA method.

Table 10. Comparison of the turbulent heat flux results at EC4

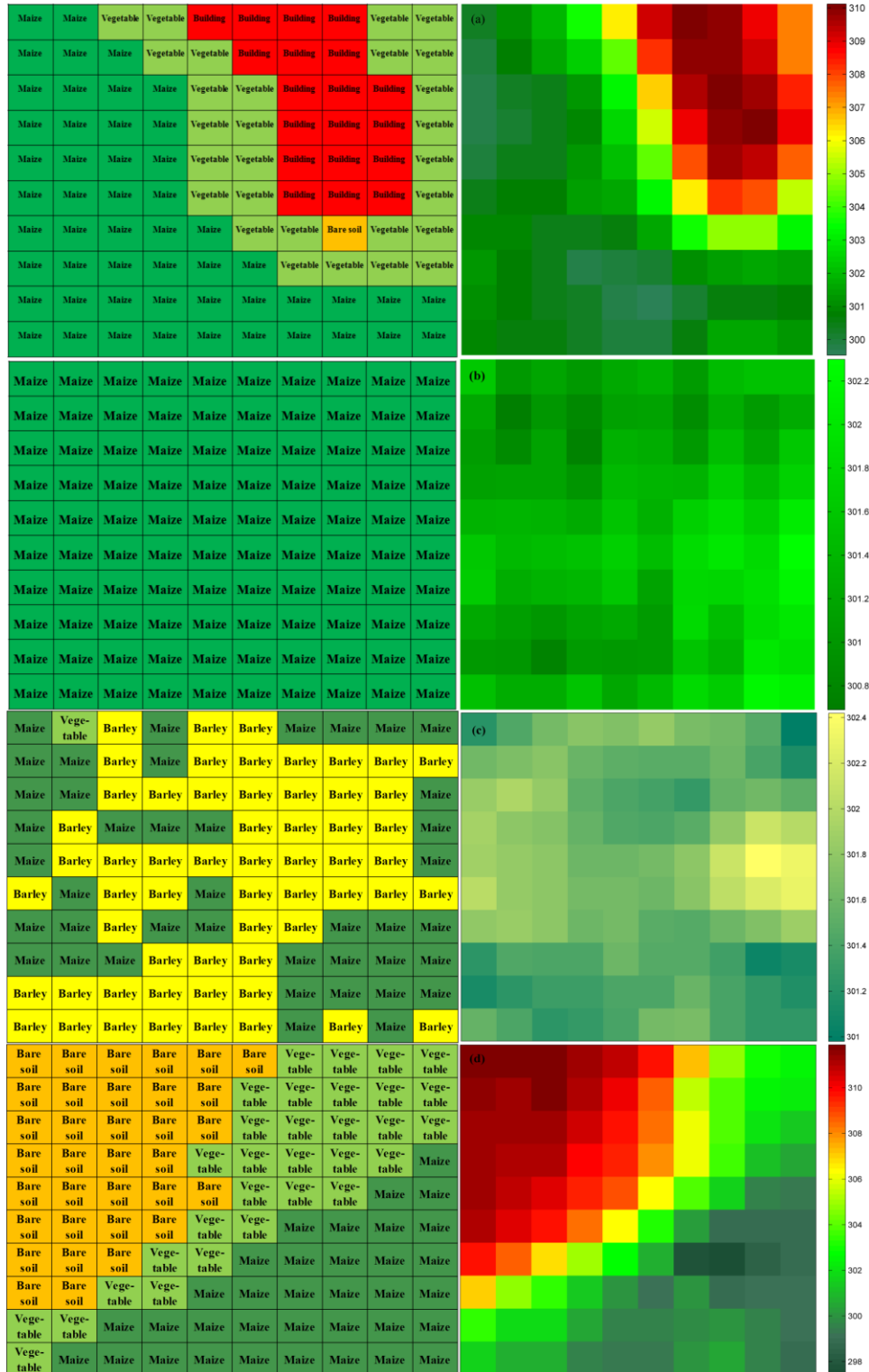
EC4		H($\text{W}\cdot\text{m}^{-2}$)				LE($\text{W}\cdot\text{m}^{-2}$)			
Date	EC	IPUS	TRFA	TSFA	EC	IPUS	TRFA	TSFA	
0619	150.65	105.86	154.71	142.13	278.55	402.60	344.05	357.79	
0630	138.32	99.91	153.53	126.88	341.98	419.83	358.12	386.07	
0708	117.04	63.47	131.79	112.16	361.16	502.60	424.85	444.01	
0727	136.41	4.87	85.99	72.33	306.53	543.48	452.01	467.96	
0803	68.97	36.51	111.73	74.76	389.63	498.21	414.67	454.23	
5	104.60	12.69	88.26	82.56	357.34	522.31	436.43	441.95	
0822	125.34	85.93	120.68	93.18	318.08	415.15	370.76	400.99	
0829	82.93	73.06	103.84	74.76	317.68	362.04	322.77	355.16	
0902	162.05	93.74	144.49	132.60	280.41	375.42	315.16	326.29	
0913	119.42	151.44	157.07	130.85	263.18	234.93	222.62	249.59	
0914	110.02	88.24	128.37	99.33	262.33	333.82	285.04	314.91	

units: $\text{W}\cdot\text{m}^{-2}$

Variable	IPUS			TRFA			TSFA		
	R^2	MBE	RMSE	R^2	MBE	RMSE	R^2	MBE	RMSE
EC4-H	0.11	-44.65	61.73	0.25	5.88	26.33	0.51	-16.93	26.54
EC4-LE	0.49	99.21	119.55	0.56	42.69	62.40	0.60	63.92	76.78

Fig. 8 shows that the classes and temperatures of 10×10 sub-pixels at 30 m correspond to the pixels with a resolution of 300 m at the EC tower. In the IPUS upscaling scheme, the 300 m pixels included buildings, maize and vegetable crops at the 30 m resolution and were identified as maize. The canopy height gap between maize and vegetables was large during our study period, resulting in the overestimation of the canopy height. For additional details, see the error analysis in section 4.4. However, because buildings corresponded with $H = 0.6R_n$ in this study, ignoring the contributions of buildings would result in the underestimation of H. Fig. 8(a) shows the temperature-sharpening results in the EC4 pixel on August 29. The temperature retrieved at 300 m scale was 303.49 K. Compared with the *in situ* measurement of 313.24 K, the temperature was underestimated at a resolution of 300 m. Even when substituting the *in situ* temperature into the ET model, the value of H reached $399.60 \text{ W}\cdot\text{m}^{-2}$ and the LE became $0 \text{ W}\cdot\text{m}^{-2}$. When substituting the *in situ* temperature into the TRFA method, H was $396.49 \text{ W}\cdot\text{m}^{-2}$ and LE was $18.7 \text{ W}\cdot\text{m}^{-2}$, indicating that the LE was underestimated and the H was overestimated with large errors. After processing by temperature sharpening, the distribution of the temperature at the 30 m resolution agreed with the classification.

1 Temperature sharpening improved the description of heterogeneity based on the thermodynamic-
 2 driven force of the turbulent heat flux. These results apply to the ET model based on the classifica-
 3 tion map and high-resolution inputs and correspond to more accurate sensible heat flux estimates.



4 **Figure 8.** Distribution of classes and temperatures over (a) EC4, (b) EC15, (c) EC11 and (d) TP on August 29, 2012

5 The land surface of EC15 was uniform and consisted of pure pixels covering maize fields.
 6 Consequently, the temperature distribution at 30 m resolution was very homogeneous, and the sur-
 7 face temperature variations were comprised within a range of 1.6 K. Table 11 shows the *in situ*
 8

validation results at EC15, for which the overall accuracy is not high due to the low LST retrieval accuracy on July 8, which is discussed in section 4.4.1. For homogeneous surfaces, the gaps between IPUS, TRFA and TSFA were not large (within $10 \text{ W}\cdot\text{m}^{-2}$), and the accuracy did not improve (MBE and RMSE did not exhibit obvious variations). Statistically sharpening the temperature may increase the uncertainty of the model results for homogeneous surfaces; however, this influence could be omitted.

Table 11. Comparison of the turbulent heat fluxes results at EC15

EC15		H ($\text{W}\cdot\text{m}^{-2}$)				LE ($\text{W}\cdot\text{m}^{-2}$)			
Date	EC	IPUS	TRFA	TSFA	EC	IPUS	TRFA	TSFA	
0619	92.55	106.60	109.25	99.81	419.47	427.19	419.99	429.98	
0630	42.37	43.99	45.51	44.67	551.73	527.12	525.17	526.09	
0708	18.34	217.53	235.48	209.90	620.95	425.71	397.49	424.86	
0727	27.68	21.22	31.11	24.30	597.76	589.58	579.43	586.47	
0803	2.33	33.32	-0.07	0.01	592.37	565.20	601.33	601.33	
0815	48.81	32.31	46.28	44.62	553.74	561.92	547.48	549.11	
0822	54.59	154.34	151.77	158.60	473.68	408.37	410.80	405.07	
0829	9.80	94.97	95.01	90.91	473.54	399.25	398.52	402.93	
0913	176.96	265.62	209.65	257.81	307.72	165.40	221.68	173.58	
0914	188.34	198.15	197.04	196.60	274.98	275.07	276.05	276.56	

units: $\text{W}\cdot\text{m}^{-2}$

Variable	IPUS			TRFA			TSFA		
	R ²	MBE	RMSE	R ²	MBE	RMSE	R ²	MBE	RMSE
EC15-H	0.40	40.64	74.64	0.33	45.93	80.81	0.40	40.36	72.88
EC15-LE	0.74	-52.11	83.48	0.71	-48.80	82.51	0.74	-49.00	81.94

The weak heterogeneous land surface at EC11 contained barley, maize and vegetables in a 300 m pixel resolution with a fractional area of 58:41:1 and was classified as barley at the 300 m resolution. The distributions of the classes and temperatures are shown in Fig. 8(c). The pixel belongs to the first conditions of heterogeneity (nonlinear vegetation density variation between sub-pixels). Table 12 shows the *in situ* validation results of EC11. The improvements in the accuracies of H and LE by temperature resampling or sharpening were not as obvious as the improvements at EC4, which contained totally different landscapes (the other inhomogeneous condition).

Theoretically, the LE from the TSFA and TRFA at EC11 should be smaller than the IPUS LE values in the energy balance system. The height of maize (ranges from 0.3 to 2 m) was generally higher than the height of barley (ranges from 0.9 to 1.1 m) in the study area from June to August. Taller vegetation resulted in larger surface roughness and smaller aerodynamic resistance, which led to larger H values and smaller LE values, and vice versa (e.g., vegetables with a canopy height of 0.2 m). When using the TSFA and TRFA methods, patch landscapes consisting of different crops, such as maize and vegetables, were considered. Thus, the LE was smaller than the IPUS LE. On June 19, the canopy height of maize was 0.74 m, which was lower than the canopy height of barley (1 m) and indicated that the H values resulted from the TRFA and TSFA methods were less than H resulted from the IPUS method. Because our validation method considered the influence of source area, the *in situ* turbulent heat flux validation results included the effects of neighboring pixels (i.e., on August 3, the turbulent heat flux values of the pixel corresponding to the location of EC11 was only assigned a weight of 37% in the source area).

The differences between the TSFA and TRFA methods were small and resulted from the LST differences between the 30 m resolution temperature-sharpening results and the LST retrieved at the 300 m resolution, but these differences were not evident at EC11. For example, on August 29, the temperature range was 1.4 K, as shown in Fig. 8(c). This temperature was even less than the temperature range at EC15 because the observation system at EC15 was a superstation with a 40 m tall tower that may cause large shadow effects and result in a relative large temperature range. Hence, the temperature sharpening effect is not obvious after aggregating the flux at the 300 m resolution under dense vegetation canopies. However, temperature sharpening can still decrease the heterogeneity that resulted from thermal dynamics.

The excess errors at EC11 was caused by the relatively low LST accuracy, with R^2 , MBE and RMSE values of 0.42, 1.59 K and 2.98 K, respectively. On August 29, the temperature retrieved at 300 m scale was 301.6 K, and the observed ground temperature was 300.20 K. The LST at the 300 m resolution was slightly overestimated. When the *in situ* temperature was substituted into the IPUS algorithm, the value of H decreased to $16.06 \text{ W}\cdot\text{m}^{-2}$ and LE became $467.43 \text{ W}\cdot\text{m}^{-2}$. When the *in situ* temperature was substituted into the TRFA scheme, the value of H was $22.43 \text{ W}\cdot\text{m}^{-2}$ and the LE was $461.58 \text{ W}\cdot\text{m}^{-2}$, which were similar to the ground observations.

Table 12. Comparison of the turbulent heat flux results at EC11

EC11		H($\text{W}\cdot\text{m}^{-2}$)				LE($\text{W}\cdot\text{m}^{-2}$)			
Date	EC	IPUS	TRFA	TSFA	EC	IPUS	TRFA	TSFA	
0619	33.94	173.69	158.12	158.18	531.46	391.60	407.42	407.40	
0630	25.03	3.29	23.12	21.37	635.22	586.37	566.48	568.28	
0708	32.29	68.17	97.16	96.13	601.98	567.73	538.77	539.81	
0727	21.42	-1.17	-1.58	-3.77	587.70	618.80	619.19	621.46	
0803	7.01	24.85	20.34	19.52	614.28	575.03	585.29	586.16	
0815	38.94	12.51	15.52	16.02	567.07	584.31	581.31	580.82	
0822	69.25	73.45	83.11	84.38	516.07	483.23	473.60	472.40	
0829	29.77	48.21	60.9	60.81	473.22	427.92	415.32	415.45	
0902	193.97	154.58	197.01	197.49	306.62	361.96	319.54	319.03	
0913	288.37	168.42	176.4	177.71	160.29	216.53	208.49	207.19	
0914	240.33	268.91	256.29	256.40	199.52	156.00	168.63	168.55	

18 units: $\text{W}\cdot\text{m}^{-2}$

Variable	IPUS			TRFA			TSFA		
	R^2	MBE	RMSE	R^2	MBE	RMSE	R^2	MBE	RMSE
EC11-H	0.61	-1.07	61.31	0.57	-0.36	63.24	0.67	-0.21	55.50
EC11-LE	0.88	-19.83	63.16	0.89	-18.12	60.02	0.90	-21.29	58.11

Another typical pixel located at the boundary of the bare soil and the oasis with no flux measurements was used to evaluate the correction effects of landscapes and temperature sharpening. The land surface of the TP contained maize, vegetables and bare soil at a fraction of 35:31:34. Table 13 shows that when neither the heterogeneity of the landscape nor the LST are considered, the relative error of LE reached $180 \text{ W}\cdot\text{m}^{-2}$. In addition, if only the LST heterogeneity is not considered, the LE relative error reached $48 \text{ W}\cdot\text{m}^{-2}$. This result also reveals that the influences of landscape inhomogeneity are greater than the influences of inhomogeneity on the LST in mixed pixels.

Table 13. Comparison of the turbulent heat flux results at TP

H ($\text{W}\cdot\text{m}^{-2}$)		LE ($\text{W}\cdot\text{m}^{-2}$)	
------------------------------------	--	-------------------------------------	--

Date	IPUS	TRFA	TSFA	IPUS	TRFA	TSFA
0619	186.31	149.73	143.98	321.04	358.22	364.79
0630	383.65	191.59	158.79	67.03	259.36	292.89
0708	498.36	240.20	204.18	0.29	259.25	293.41
0727	276.79	136.06	84.01	206.52	347.64	402.23
0803	214.14	75.45	53.72	252.37	392.08	416.41
0815	214.14	98.24	72.05	252.37	368.64	393.68
0822	436.48	369.28	276.70	0.00	67.79	162.80
0829	235.29	117.16	67.21	183.62	302.41	356.75
0902	423.61	212.15	180.92	0.00	211.77	241.36
0913	338.00	285.04	216.26	0.00	53.62	122.58
0914	270.44	148.20	100.19	115.19	238.43	286.51

1 units: $W \cdot m^{-2}$

Variable	IPUS			TRFA		
	R ²	MBE	RMSE	R ²	MBE	RMSE
TP-H	0.62	174.47	185.49	0.95	42.28	48.01
TP-LE	0.71	-175.91	186.63	0.97	-43.11	49.04

2 4.3.2. Comparison of the TRFA and IPUS methods

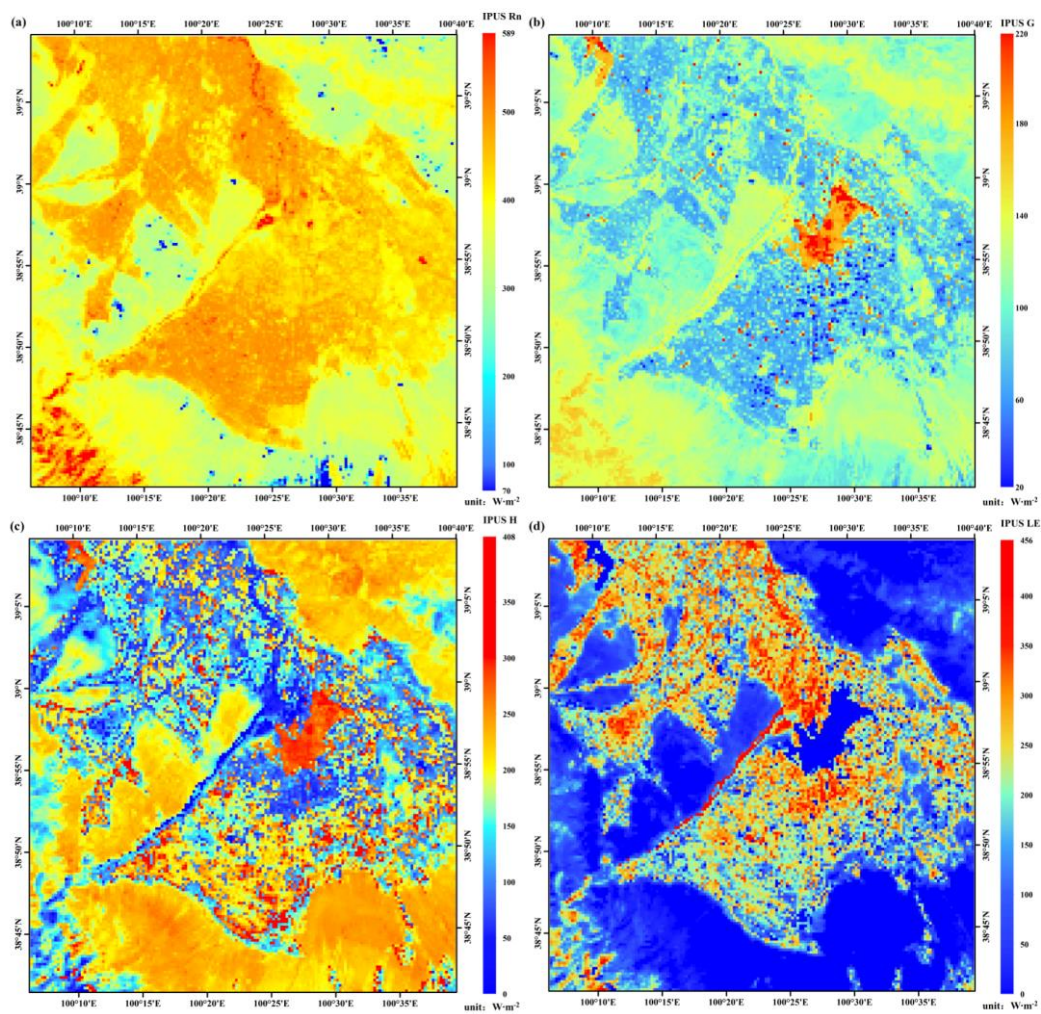
3 Using data of September 13 as an example, the spatial distributions of the four components of
4 the energy balance calculated by the IPUS and TRFA methods are shown in Fig. 9 and Fig. 10,
5 respectively. TSFA minus IPUS and TSFA minus TRFA, which display the spatial distributions of
6 the scale effect, are shown in Fig. 11. Scatterplots of TSFA versus IPUS and TRFA are shown in
7 Fig. 12.

8 A comparison of Fig. 6 with Fig. 9 shows that the spatial distributions of the fluxes greatly
9 change, except for R_n . The TSFA results are synoptically smoother than the IPUS results because
10 the land cover types and temperature distributions in mixed pixels are not considered in IPUS. For
11 example, the boundary between the oasis and uncultivated land becomes a belt of intermediate G,
12 H and LE because these mixed pixels include uncultivated land and vegetation. However, mixed
13 pixels are classified as the dominant land use type in the parameterization process of IPUS. This
14 result overlooks the contributions of heat flux from complex land use types and overestimates or
15 underestimates the turbulent heat flux by approximately $50 W \cdot m^{-2}$. Since the TSFA can integrate the
16 effects of these land areas and reveals the relative actual surface conditions, the heat flux results of
17 TSFA vary less dramatically than those of IPUS, as shown in the figures. The results are similar in
18 the oasis area.

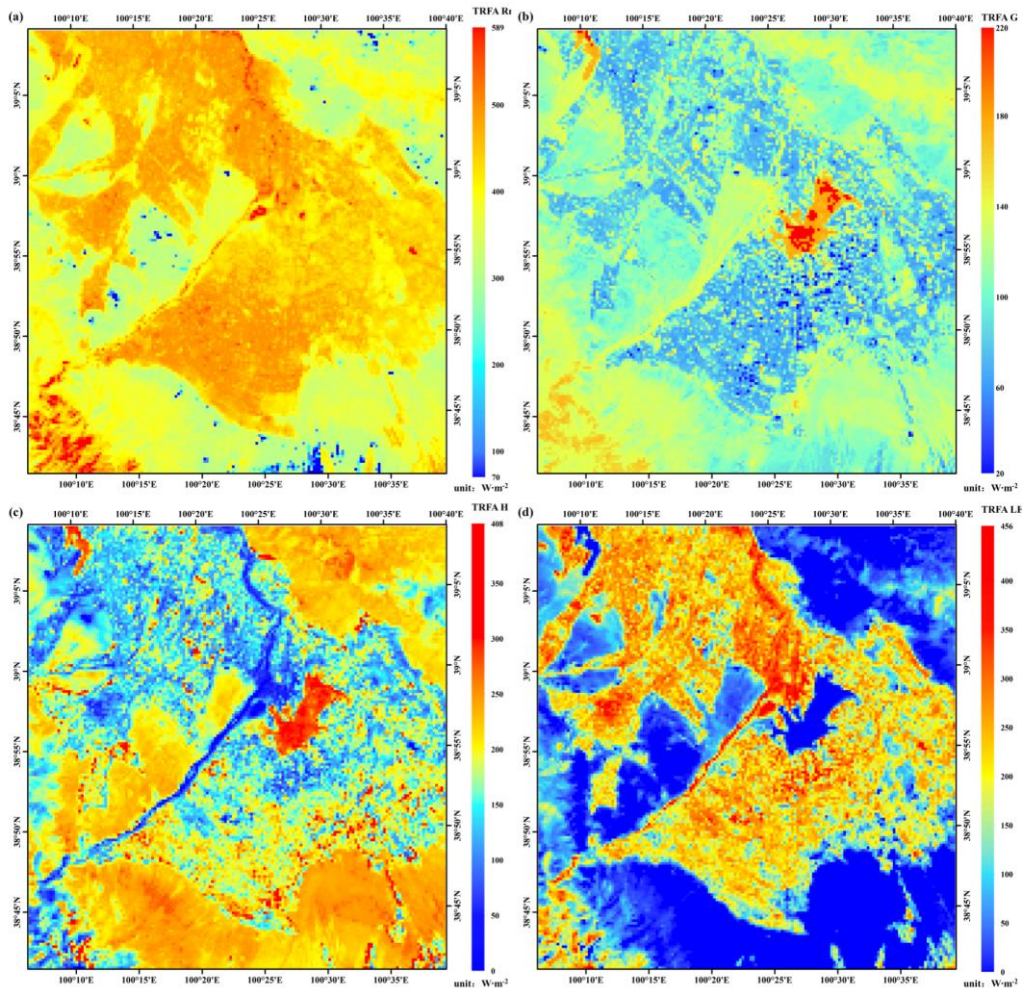
19 Based on Fig. 6 and Fig. 10, the TRFA and TSFA methods are similar. Because the TRFA
20 method considers the sub-pixel landscapes that could be significant source of error in the ET models,
21 the difference between the TSFA and TRFA methods is mainly resulted from the differences between
22 the sharpened LST and retrieved, resampled LST of sub-pixels at the 30 m resolution. In addition,
23 the bias between the TSFA and TRFA is not as obvious as the bias between the TSFA and IPUS
24 methods, as shown in Fig. 11(c)-(f). Furthermore, Fig. 11(f) shows that the LEs calculated by using
25 the TSFA method in most oasis areas were slightly greater than the LEs calculated by using the
26 TRFA method, which yielded values of approximately $20 W \cdot m^{-2}$.

27 The quadrangular with a relatively unstable bias shown in Fig. 11(a) is caused by the L_d that

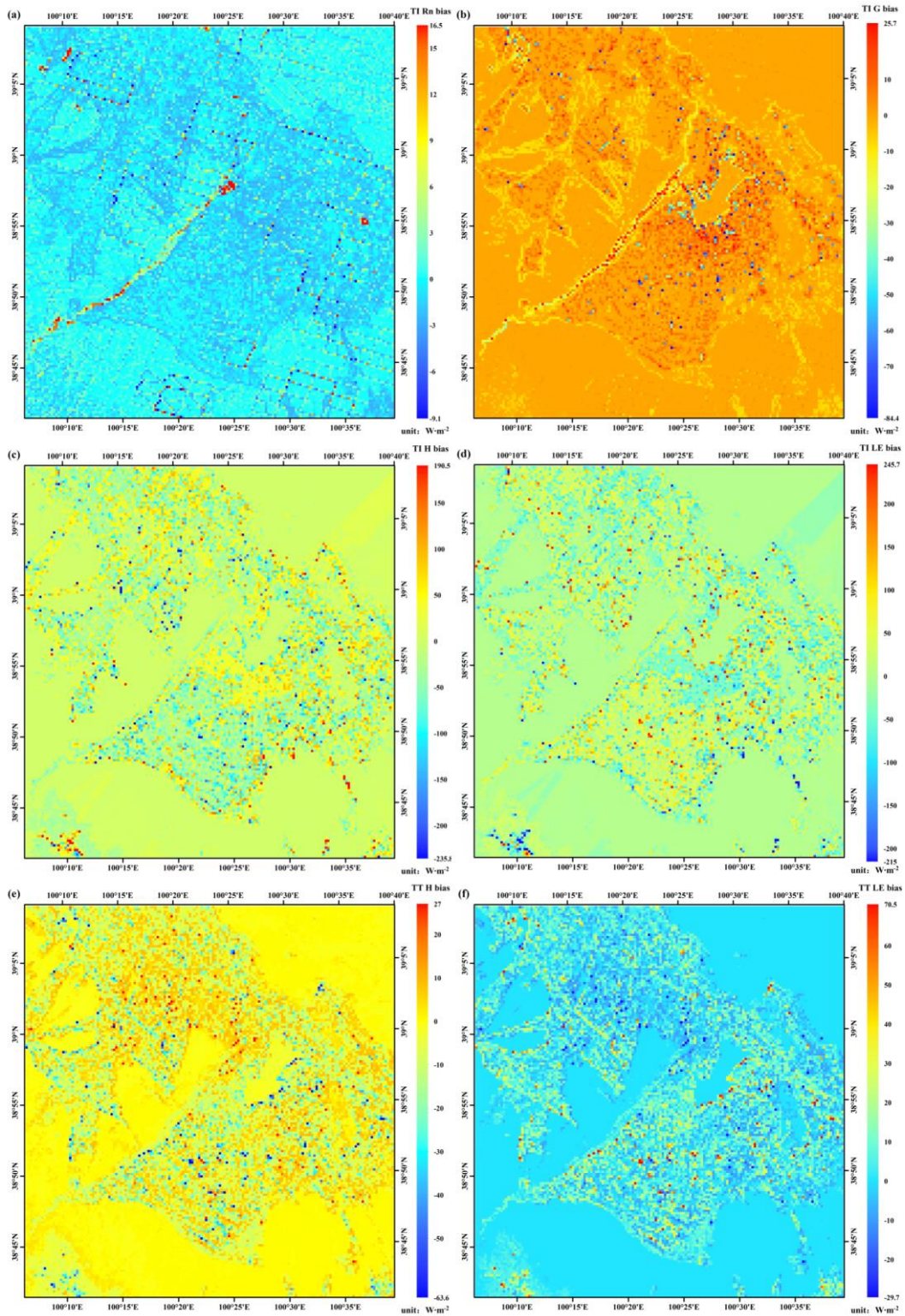
1 was calculated from the MOD05 water vapor product which exists quadrangular even after prepro-
2 cessing the instrument malfunction gap. In Fig. 11, the differences of the four energy components
3 of the pure pixels between these three methods are within $5 \text{ W}\cdot\text{m}^{-2}$, and the mixed pixels have dif-
4 ferent ranges.



5
6 **Figure 9.** Maps of the four energy components, (a) R_n , (b) G , (c) H and (d) LE , calculated using the IPUS method
7 on September 13, 2012



1
 2 **Figure 10.** Maps of the four energy components, (a) R_n , (b) G , (c) H and (d) LE , calculated using the TRFA method
 3 on September 13, 2012



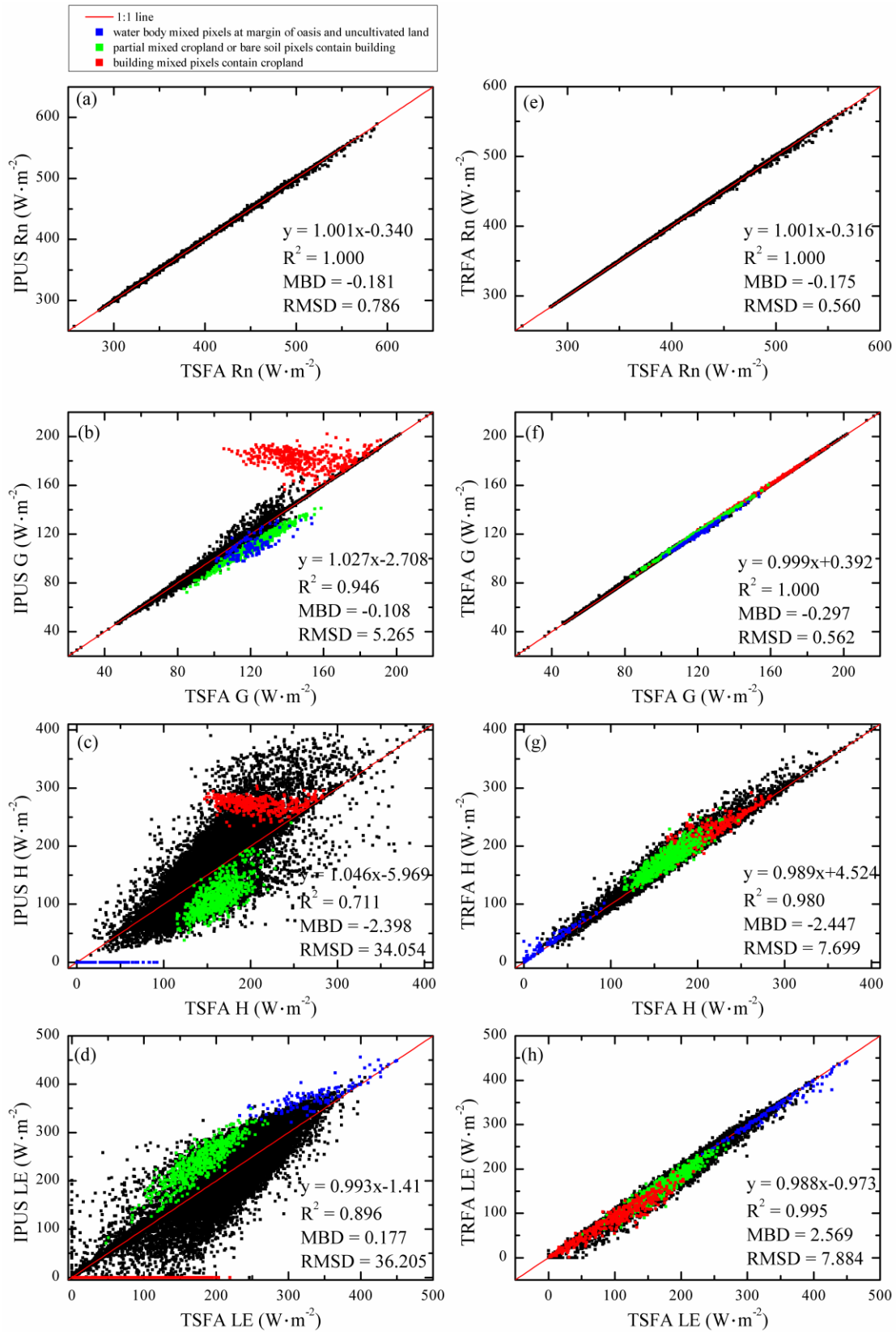
1

2

Figure 11. Maps of the bias of the energy balance components calculated using the TSFA method minus the IPUS

3

method: (a) R_n , (b) G , (c) H , (d) LE , and TSFA minus TRFA: (e) H and (f) LE



1

2 **Figure 12.** Scatter plots between the TSFA and IPUS results: (a) R_n , (b) G, (c) H and (d) LE; and TSFA and TRFA
 3 results: (e) R_n , (f) G, (g) H and (h) LE. MBD and RMSD are the mean bias deviation and root mean square deviation
 4 between the TSFA and IPUS results, respectively

5 Fig. 12 shows the scatter plots between the results of the TSFA method and the other two

1 methods for all four energy balance components. Fig. 11(a)(e) shows that R_n does not vary much
2 between the three methods and the scatter is centralized around the 1:1 line. However, regarding the
3 spatial scale effect, the differences in G , H and LE calculated by using the IPUS and TSFA meth-
4 ods are obvious. The scatter plots disperse at the mixed pixels, and the differences between the
5 TRFA and TSFA results are relatively smaller. When using the TSFA method, the temperature sharp-
6 ening results can be divided into results that are higher and lower than the LST retrieved at 300 m.
7 Compared to the LST retrieved at 300 m when using the TRFA method, a higher LST is counterbal-
8 anced by a lower LST when calculating H using the TSFA. Thus, the effect of temperature hetero-
9 geneity is neutralized in this case. This observation is potentially resulted from the temperature-
10 sharpening algorithms because they tend to overestimate the sub-pixel LST for cooler landscapes
11 and underestimate the sub-pixel LST for warmer areas in the image (Kustas et al., 2003).

12 However, LE is calculated as a residual; thus, the difference of LE is resulted from G and H .
13 When the 300 m mixed pixels contained various types of landscapes, they were categorized as one
14 type of landscape in the IPUS method and a single temperature value was used to evaluate the ther-
15 mal dynamic effects when using the TRFA method. Pixels with highly different G , H and LE val-
16 ues are mainly distributed near the mixed pixels, as shown in Fig. 10. An explanation for these
17 deviations is provided below.

18 The parameterization of G and H are based on the land cover type. For example, for build-
19 ings, $G = 0.4R_n$ (Kato and Yamaguchi, 2005) (which is usually greater than the G of vegetation
20 and bare soil deduced from Eq.(9)) and $H = 0.6R_n$, and for water, $G = 0.226R_n$ and $LE = R_n -$
21 G . From the land cover map shown in Fig. 4, four major classes exist in the study area: buildings
22 with a high H , uncultivated land with a relatively high H , cropland with a relatively low H , and
23 water with $H = 0$.

24 (1) If a pixel contains cropland and buildings and is categorized as cropland, the building area
25 within the pixel is ignored in the IPUS method. In this case, G and H are underestimated and LE
26 is overestimated. In addition, after considering the landscapes using the TRFA method, the LE is
27 underestimated and H is overestimated because the pixels contain buildings that are still reflected
28 indistinctly by LST at 300 m because the detailed temperature heterogeneity cannot be represented
29 by the TRFA method. These points are shown in green in Fig. 11. However, if the pixel is categorized
30 as built-up, the building area within a pixel is exaggerated, which causes G and H to be overesti-
31 mated and LE to be underestimated when using the IPUS method. This situation is similar to that
32 illustrated by the green points associated with the TRFA results and is shown by the red points in
33 Fig. 11.

34 (2) At the boundary of the oasis and uncultivated land, the mixed pixels are divided into
35 cropland, LE is overestimated, G and H are underestimated in the IPUS method, and vice versa.
36 LE is also overestimated in the pixels containing water and other types of land cover (generally
37 bare soil in our study area). These pixels are categorized as water and are shown as blue points in
38 Fig. 11. Some of the blue LE points calculated by using the TSFA method are slightly smaller than
39 those calculated using the TRFA method for pixels containing vegetation. At noon, the temperature
40 of vegetation in those pixels is lower than that of water bodies.

41 (3) In mixed pixels that contain various crops, such as maize and vegetables, LE is underesti-
42 mated if the area of maize within the pixel is overestimated because the canopy height of the maize
43 is taller than that of vegetables. This relationship results in the overestimation of H when using the
44 IPUS and TRFA methods. In addition, G depends on the FVC values of the crops when using the

1 IPUS method. Moreover, G depends on R_n when using the TRFA method and is nearly identical
 2 to the values of G obtained using the TSFA method.

3 At the study area, we compared the TRFA and IPUS methods to quantify the ability of the
 4 TSFA method to simulate the heterogeneities of the land surface on September 13 (see Table 14). In
 5 pure pixels, the LE biases among the IPUS, TRFA and TSFA methods were small. In mixed pixels,
 6 the LE bias between the TSFA and IPUS methods varied from 35.36 to 65.66 $W \cdot m^{-2}$, and the bias
 7 between the TSFA and TRFA methods varied from 4.41 to 22.53 $W \cdot m^{-2}$. More class types in mixed
 8 pixels correspond to larger biases. Table 15 shows the bias of the mixed pixels that contain buildings
 9 and bare soil between the three methods. In mixed pixels with buildings, the IPUS and TRFA meth-
 10 ods generally underestimated LE and had large bias values compared to those of the TSFA method.
 11 In mixed pixels without buildings and bare soil, the bias between TRFA (or IPUS) and TSFA was
 12 relatively small, which indicates that the landscape and temperature inhomogeneity were accounted
 13 for by the TSFA method. The aforementioned analyses demonstrate that the TSFA method can con-
 14 sider the heterogeneous effects of mixed pixels.

15 **Table 14.** Comparison of the latent heat flux in pixels containing different numbers of class types

Number of class types in pixels	IPUS ($W \cdot m^{-2}$)			TRFA ($W \cdot m^{-2}$)			Pixel number
	R ²	MBD	RMSD	R ²	MBD	RMSD	
1	1.00	0.21	0.21	1.00	0.05	0.61	11,398
2	0.85	-7.18	35.36	1.00	-0.35	4.41	8212
3	0.66	-2.32	52.55	0.98	-7.33	12.56	4762
4	0.49	1.88	65.66	0.96	-11.56	16.55	2824
5	0.98	-30.92	62.69	0.96	-16.90	22.53	4

16 Notes: The number of class types in mixed pixels represents the number of classification types that were con-
 17 tained in the pixels. For example, 1 represents the pure pixels, 2 represents mixed pixels containing two land use
 18 types, etc. MBD and RMSD are the mean bias deviation and root mean square deviation, respectively, between the
 19 TSFA results and the TRFA and IPUS results.

20 **Table 15.** Comparison of the latent heat fluxes of typical mixed pixels

Types of mixed pixels	IPUS ($W \cdot m^{-2}$)			TRFA ($W \cdot m^{-2}$)			Pixel number
	R ²	MBD	RMSD	R ²	MBD	RMSD	
Mixed pixels containing buildings	0.58	-1.02	61.94	0.97	-9.64	14.66	4918
Mixed pixels do not containing buildings	0.81	-5.49	39.21	0.99	-2.12	7.60	10,884
Mixed pixels containing bare soil	0.73	-1.52	49.04	0.98	-5.96	11.86	9049
Mixed pixels do not containing bare soil	0.65	-7.55	45.28	0.98	-2.46	7.83	6753

21 Considering the landscapes and inhomogeneous distribution of LST, the TSFA method ensures
 22 that none of the end members (30 m pixel) are ignored or exaggerated. Thus, the distribution of LE
 23 calculated using the TSFA method is smoother and more rational than the distributions of LE cal-
 24 culated using the other methods. At the regional scale, the TSFA method describes the heterogeneity
 25 of the land surface more precisely. The degree of achievable estimation accuracy is discussed here-
 26 after.

27 4.4. Error analysis

28 Since LE is calculated as a residual term in the energy balance equations, the sensitivity of H
 29 was analyzed first. Land surface variables (including LST, LAI, canopy height, and FVC) and me-
 30 teorological variables including wind speed, air temperature, air pressure and relative humidity are

the major factors for H sensitive analysis. Fig. 13 presents a case of sensitivity analysis results for H. In this case, LST is 303.9 K, and it ranges from 298.4~309.4 K with a step size of 0.5 K, LAI is set to 1.4 and it ranges from 0.14~2.66 with a step size of 0.14. Canopy height is 1 m and it ranges from 0.1~1.9 m with a step size of 0.1 m. Additionally, FVC=0.5, wind speed $u=2.48 \text{ m}\cdot\text{s}^{-1}$, air temperature $T_a=297.9 \text{ K}$, air pressure = 97.2 kPa, and RH=40.29%. In addition, the land cover is maize, and the reference H is $230.2 \text{ W}\cdot\text{m}^{-2}$.

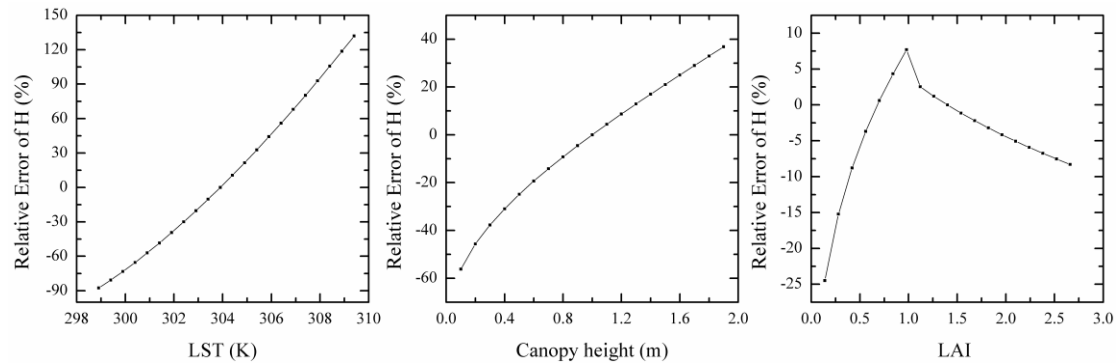


Figure 13. Sensitivity analysis of the surface variables for sensible heat flux

The air pressure is stable over a short period and has little effect on the ET results. Although “excess resistance” was calculated from the friction velocity, the meteorological data were provided by ground observations; thus, the meteorological data are relatively accurate. As shown in Fig. 13, LAI, canopy height and LST are sensitive variables.

The parameterization of the momentum roughness length indicates that H is sensitive to LAI, with decreasing sensitivity when the LAI is greater than 1. When the LAI is less than 1, the momentum roughness length increases as the LAI increases, and turbulent exchange are enhanced. However, when the LAI is greater than 1, the plant canopy is regarded as a continuum that is not a sensitive variable. Because our study area is dominated by agriculture and the study period extended from July to September, the crops in the HRB middle stream grew quickly, thus, the LAI was usually greater than 1. Thus, LST and canopy height are the main sources of error.

4.4.1. Errors in LST

As shown in Fig. 13, 1 K LST bias would result in 21% error of H while H is $230.2 \text{ W}\cdot\text{m}^{-2}$. However, the sensitivity of the LST is unstable and depends on the strength of the turbulence. The strength of the turbulence determines the mass and energy transport and the resistance of heat transfer, which influences the sensitivity to the LST. A weaker turbulence corresponds to a weaker LST sensitivity, and vice versa.

A sensitivity analysis of LE induced by LST was also performed. In order to exclude the influence of other factors, stations were chosen with homogeneous landscapes within coarse pixels. These results are shown in Table 16. The LE results obtained from the observed LST are consistent with the *in situ* observations and have less bias. LE was overestimated when the LST was underestimated, and vice versa. Because the magnitude of LE was greater than that of H, the relative error of LE was less than the relative error of H. However, 1 K of LST bias resulted in an average LE error of $30 \text{ W}\cdot\text{m}^{-2}$, which is consistent with the sensitivity analysis of H shown in Fig. 13. Specifically, 1 K of LST bias would result in an LE biases of $8.7 \text{ W}\cdot\text{m}^{-2}$ (in desert, SSW) to $84.4 \text{ W}\cdot\text{m}^{-2}$ (in oasis, EC8), which indicates that the sensitivity of LST is unstable.

Table 16. The results of the LST error analyses at the stations with homogeneous landscapes

Station	Date	Re- trieved LST (K)	Ob- served LST (K)	LST bias (K)	EC-LE (W·m ⁻²)	LE from retrieved LST (W·m ⁻²)	LE from observed LST (W·m ⁻²)	LE relative error (%)	H relative error (%)
EC8	0619	304.92	301.74	3.18	415.89	321.80	399.78	-22.62	68.58
EC7	0630	302.5	299.35	3.15	611.22	453.59	557.97	-25.79	886.08
EC10	0708	303.58	300.5	3.08	617.83	504.44	549.53	-18.35	390.24
EC15	0708	303.55	300.13	3.42	620.95	425.71	603.73	-31.44	450.57
EC7	0727	298.87	300.55	-1.68	577.59	643.56	566.62	11.42	-132.47
SSW	0727	307.86	316.82	-8.96	119.35	238.07	78.43	99.48	-60.36
EC8	0822	299.58	297.77	1.81	543.56	416.23	467.42	-23.42	88.59
EC10	0822	301.61	298.04	3.57	503.82	398.82	513.67	-20.84	138.61
EC15	0822	300.59	297.69	2.9	473.68	408.37	495.49	-13.79	129.60
EC8	0829	301.54	300.44	1.1	514.31	402.93	428.78	-21.66	63.91
EC15	0829	301.41	299.84	1.57	473.54	399.25	459.66	-15.69	182.34
SSW	0902	304.9	303.42	1.48	226.88	127.96	149.83	-43.60	11.36

1 Notes: “LST bias” is calculated as the retrieved LST minus the observed LST; “EC-LE” is the *in situ* latent heat flux;
2 “LE relative error” is the relative error between the retrieved and observed LST and is expressed as ((LE from
3 retrieved LST)-(LE from observed LST))/(LE from observed LST)×100% and “H relative error” is calculated in the
4 same way.

5 4.4.2. Errors in canopy height

6 In this paper, canopy height was obtained from a phenophase and classification map. Thus, the
7 accuracy of the canopy height was mainly dependent on the classification accuracy and plant growth
8 state. Even within the same region, the canopy height of a crop can differ due to differences in
9 seeding times and soil attributes, such as soil moisture and fertilization.

10 The land use type was orchard at EC17. However, in our land classification map, the land use
11 at EC17 was other crops, which includes vegetables and orchards. Thus, it was difficult to set the
12 canopy height. In our study area, most of the other crops were vegetables (canopy height of 0.2 m),
13 and the height of the orchard was approximately 4 m; thus, a value of 0.2 m would overestimate the
14 LE. The LE estimations with incorrect canopy heights and correct orchard canopy height at EC17
15 are shown in Table 17. The days of large LST bias were removed, and the bias between the model
16 and ground observations decreased. The excess errors were caused by errors in the LST and land
17 use, such as buildings and maize in the mixed pixels.

18 **Table 17.** The results of the canopy height error analyses at EC17

Date	EC-LE (W·m ⁻²)	LE from incorrect canopy height (W·m ⁻²)	LE-I relative error (%)	LE from correct canopy height (W·m ⁻²)	LE-C relative error (%)
20120815	499.62	562.06	12.50	521.83	4.45
20120822	366.27	519.01	41.70	396.54	8.26
20120902	377.96	471.68	24.80	336.52	-10.96
20120914	465.38	352.78	-24.20	258.07	-44.55

19 Notes: “LE-I relative error” is the relative error between the LE from incorrect canopy height and observed LE and
20 is expressed as ((LE from incorrect canopy height)-(EC-LE))/(EC-LE)×100%, “LE-C relative error” is the relative

1 error between the LE from correct canopy height and observed LE and is expressed as $((LE \text{ from correct canopy}$
2 $\text{height}) - (EC - LE)) / (EC - LE) \times 100\%$.

3 Except for the error source discussed previously, the following sources of error were unavoid-
4 able:

5 (1) Although the remotely sensed turbulent heat flux is instantaneous, the EC data are averaged
6 over time. Thus, the time scales do not match in the validation.

7 (2) The calibration coefficients of the HJ-1B satellite's CCD and IRS drifts because of instru-
8 ments aging.

9 (3) Geometric correction causes half-pixel bias equal to or less than the deviation of the artifi-
10 cially subjective interpretation.

11 A one-source model and simplified parameterization schemes were used in this paper to deter-
12 mining surface roughness lengths and heat transfer coefficients. The one-source model combines
13 soil evaporation and plant transpiration and assumes that SPAC is a one-source continuum. This
14 assumption is reasonable when the surface is densely covered by vegetation but relies on the accu-
15 racy of the difference between the LST and air temperature, as previously mentioned. When a one-
16 source model is applied to an area covered by sparse vegetation, such as semi-arid or arid areas, this
17 assumption is irrational.

18 **5. Discussions**

19 The TSFA describes the surface heterogeneity much better than the IPUS and TRFA. The IPUS
20 aggregates the land surface variables from 30 m to 300 m, which results in the loss of land surface
21 details and leads to the scale effects. Although the TRFA uses 30 m information from VNIR bands
22 and partially decreases the heterogeneity, it treats the pivotal variable LST as homogeneous at 300
23 m resolution, which results in considerable error. In summary, the advantages of the TSFA method
24 are described as follows:

25 (1) The temperature sharpening algorithm in TSFA is capable of decreasing the influences of
26 the heterogeneity of the LST, which is consistent with results from previous studies (Kustas et al.,
27 2003; Bayala and Rivas, 2014; Mukherjee et al., 2014). As analyzed in section 4.3, the non-consider-
28 ation of the heterogeneity of LST in mixed pixels is ill-founded and causes errors when estimating
29 ET.

30 (2) In the one-source energy balance model, different parameterization schemes were em-
31 ployed for different landscapes. In the IPUS, a single land cover is assigned to a mixed pixel, which
32 results in a large error. However, the TSFA method is used to calculate the surface flux at 30 m and
33 is aggregated to 300 m using the area-weighting method, which considers all of the sub-pixel land-
34 scapes and improves the accuracy.

35 Some problems exist in the temperature-sharpening algorithms. The temperature-downscaling
36 method used in this paper caused "boxy" anomalies in parts of the sharpened temperature fields in
37 large pixels because of the constant residual term, $\Delta\hat{T}_{300}$, in Eq. (3) within large pixels. This situa-
38 tion also occurred in the temperature-sharpening algorithm proposed by Agam et al. (2007). In ad-
39 dition, our temperature sharpening algorithm tends to overestimate the sub-pixel LST for cooler
40 landscapes and underestimate the sub-pixel LST for warmer areas (Kustas et al., 2003). This inac-
41 curate estimation causes errors that are difficult to evaluate when estimating the turbulent heat flux.
42 For example, the small turbulent heat flux bias between TSFA and TRFA was caused by a counter-
43 balancing effect as analyzed in section 4.3.1. Additional temperature sharpening algorithms under

1 heterogeneous surfaces should be evaluated using real datasets when applied in ET models (Ha et
2 al., 2011).

3 The retrieval methods of land surface variables were validated against in other areas. For ex-
4 ample, the albedo algorithm was previously applied to retrieve Global Land Surface Satellite
5 (GLASS) Products (Liang et al., 2014), the LST retrieval algorithm was validated in the Haihe River
6 Basin in northern China (Li et al., 2011a), and the soil heat flux correction algorithm was validated
7 in the GAME-Tibet campaign (Yang and Wang, 2008). Since the surface of the Heihe River Basin
8 is very heterogeneous, additional comparisons of our algorithm in other areas would be helpful.

9 In addition, to correct the discrepancy between remotely sensed radiative surface temperature
10 and aerodynamic temperature at the source of heat transport, a brief and well performed parameter-
11 ization scheme (under uniformly flat plant surface) of “excess” resistance was used to calculate the
12 aerodynamic resistance of heat transfer (Jiao et al., 2014). Since our study is based on mixed pixels,
13 multiple parameterization methods should be compared to select the optimum method.

14 Because of the sensitive variables of the one-source energy balance model used in this paper,
15 the accuracies of the LST and canopy height greatly influenced the turbulent heat flux. HJ-1B IRS
16 has a single-thermal channel, and the single-channel LST-retrieving algorithm may be unstable un-
17 der wet atmospheric conditions (water vapor contents higher than 3 g/cm²) (Li et al., 2010a), which
18 may create a bottleneck for ET estimations by HJ-1B. The canopy height is a priori knowledge
19 based on phenophase classifications and would influence the accuracy of the surface roughness
20 calculation. Multi-source remote sensing data could be used to improve the accuracy of calibrations
21 and land surface variable estimation. Active microwave and LiDAR data (Colin and Faivre, 2010)
22 could be used to obtain the canopy height, which would decrease the dependence on the accuracy
23 of the classification.

24 The energy balance closure has a significant influence on the evaluation of the model calcu-
25 lated heat flux results. In our study area, the EC energy balance closure ratio was greater than 0.75
26 (Liu et al., 2011b). Studies have shown that not-captured low-frequency eddies (Von Randow et al.,
27 2008), extension of averaging time (Charuchittipan et al., 2014) and lack of an accurate accounting
28 of heat storage terms (Meyers and Hollinger, 2004) are potential reasons for the energy imbalance
29 and so forth. The conserving Bowen ratio and residual closure technique are often used to force
30 energy balance. We chose the residual closure method at last because the conserving Bowen ratio
31 method yields irrational sensible heat flux due to small or negative Bowen ratios (large LEs due to
32 the “oasis effect”) in the oasis-desert system. Energy balance closure was problematic at times for
33 turbulent flux system and tended to be associated with significant discrepancies in LE (Prueger et
34 al., 2005).

35 Since a footprint model was used in the validation, the footprints discrepancies between *in situ*
36 measurements and remote sensing pixel may cause biases. For example, model validation results
37 were calculated based on the relative weights of the footprint model and multiplied by the heat flux
38 results of the coarse pixels in the source area from the upwind direction. However, the heat fluxes
39 of coarse pixels included the contributions of non-overlapped sub-pixels within the coarse pixel.
40 These pixels are influenced by the heterogeneity of underlying surface, it would cause uncertainties
41 in the validation.

42 **6. Conclusion**

43 The effects of surface heterogeneity in ET estimation have been studied here by employing the

1 IPUS, TRFA and TSFA methods over heterogeneous surface. Compared to the IPUS and TRFA
 2 methods, the TSFA method exhibits more consistent agreement with *in situ* measurements (energy
 3 balance forced by the residual closure method) based on the footprint validation results. The IPUS
 4 approach does not consider surface heterogeneity at all, which causes significant error in the heat
 5 fluxes (i.e., $186 \text{ W}\cdot\text{m}^{-2}$). The TRFA considers heterogeneity of landscapes besides LST heterogene-
 6 ity, with a heat flux error (i.e., $49 \text{ W}\cdot\text{m}^{-2}$) that is less than that of IPUS. However, this error is non-
 7 negligible. As a sensitive variable of the ET model, canopy height is mainly determined by classifi-
 8 cation, and the application of classification at a 30 m resolution can improve the accuracy of the
 9 canopy height. Additionally, the sharpened surface temperature at a resolution of 30 m decreases
 10 the thermodynamic uncertainty caused by the land surface. The TSFA method can capture the het-
 11 erogeneities of the land surface and integrate the effects of landscapes in mixed pixels that are ne-
 12 glected at coarse spatial resolutions.

13 HJ-1B satellite data have advantages because of their high spatiotemporal resolution and free
 14 access. Because the satellites are still in operation, the long-term data are promising for applications
 15 of monitoring energy budgets.

16 Acknowledgements

17 The authors would like to thank Dr. Franz Meixner of the Max Planck Institute for Biogeo-
 18 chemistry in Mainz and Dr. Albrecht Neftel of the Agroscope Research Station in Zurich for provid-
 19 ing the footprint calculation tool. We are grateful to the research team of Professor ShaoMin Liu at
 20 Beijing Normal University for providing eddy covariance and automatic meteorological station data.
 21 This study was supported by the Special Fund from the Chinese Academy of Sciences (KZZD-EW-
 22 TZ-18) and the Chinese Natural Science Foundation Project (grant no. 41371360). The authors
 23 thank Bo Zhong at Institute of Remote Sensing and Digital Earth, Chinese Academy of Sciences for
 24 his very helpful comments and many corrections. Generous help for revising the paper was provided
 25 by the editors and reviewers.

26 Appendix

Notation		Application (for calculating)
6S radiation transfer mode	Second Simulation of a Satellite Signal in the Solar Spectrum radiation transfer mode	Albedo, S_d
α	Surface broadband albedo	S_d , R_n
ABT	At-nadir brightness temperature (K)	L_d
AMS	Automatic meteorological station	
AOD	Aerosol optical depth	S_d
BRDF	Bidirectional reflectance distribution function	α
CCD	Charge-coupled device	
CV	Coefficient of variation	Sharpened LST
EC	Eddy covariance	
FVC	Fractional vegetation coverage	LSE, G, LAI
G	Soil heat flux ($\text{W}\cdot\text{m}^{-2}$)	
$G(\theta)$	G function, Foliage angle distribution	LAI
H	Sensible heat flux ($\text{W}\cdot\text{m}^{-2}$)	

HRB	The Heihe River Basin	
IPUS	Input parameter upscaling scheme	
IRS	Infrared scanner	
L_d	Downward atmospheric longwave radiation ($W \cdot m^{-2}$)	R_n
LSE/ϵ	Land surface emissivity	LST
ϵ_v/ϵ_g	The vegetation/ground emissivity	
LST/T_{rad}	Land surface temperature/Surface radiation temperature (K)	H
MBE/MBD	Mean bias error (deviation)	
NCEP	National Centers for Environmental Prediction	LST
NDVI/NDVI ₃₀	Normalized difference vegetation index	FVC, Sharpened LST
NDVI ₃₀₀	300 m NDVI aggregated from NDVI	Sharpened LST
NDVI _s /NDVI _v	Normalized difference vegetation index of bare soil/fully covered vegetation	FVC
$P(\theta)$	Angular distribution of the canopy gap fraction	LAI
r_a	Aerodynamic resistance ($s \cdot m^{-1}$)	H
r_{ex}	“Excess” resistance ($s \cdot m^{-1}$)	heat transfer resistance
R_n	Net radiation ($W \cdot m^{-2}$)	
RMSE/RMSD	Root mean square error (deviation)	
S_d	Downward shortwave radiation ($W \cdot m^{-2}$)	R_n
SPAC	The soil-plant-atmosphere continuum	
SZA	Solar zenith angle	S_d
T_a	Air temperature (K)	H
T_{aero}	Aerodynamic surface temperature obtained by extrapolating the logarithmic air-temperature profile to the roughness length for heat transport (K)	H
TOA	Top of the atmosphere	
TOMS	Total ozone mapping spectrometer	S_d
TRFA	Temperature resampling and flux aggregation	
TSFA	Temperature sharpening and flux aggregation	
ULR	Upward longwave radiation ($W \cdot m^{-2}$)	R_n
USR	Upward shortwave radiation ($W \cdot m^{-2}$)	R_n
VNIR	Visible/near-infrared	
VZA/ θ	View zenith angle	L_d , LAI

1 References

- 2 Agam, N., Kustas, W. P., Anderson, M. C., Li, F., and Colaizzi, P. D.: Utility of thermal s
3 harpening over Texas high plains irrigated agricultural fields, *J. Geophys. Res.-Atmos.*, 112, D1
4 9110, doi:10.1029/2007JD008407, 2007.
- 5 Allen, R., Tasumi, M., and Trezza, R.: Satellite-Based Energy Balance for Mapping Evapo
6 transpiration with Internalized Calibration (METRIC)—Model, *J. Irrig. Drain. E.-ASCE*, 133, 38
7 0-394, 10.1061/(ASCE)0733-9437(2007)133:4(380), 2007.
- 8 Ambast, S. K., Keshari, A. K., and Gosain, A. K.: An operational model for estimating R
9 egional Evapotranspiration through Surface Energy Partitioning (RESEP), *Int. J. Remote Sens.*,
10 23, 4917-4930, 10.1080/01431160110114501, 2002.
- 11 Bastiaanssen, W. G. M., Menenti, M., Feddes, R. A., and Holtslag, A. A. M.: A remote s
12 ensing surface energy balance algorithm for land (SEBAL). 1. Formulation, *J. Hydrol.*, 212–213
13 , 198-212, [http://dx.doi.org/10.1016/S0022-1694\(98\)00253-4](http://dx.doi.org/10.1016/S0022-1694(98)00253-4), 1998.
- 14 Bateni, S. M., and Liang, S.: Estimating surface energy fluxes using a dual-source data as
15 simulation approach adjoined to the heat diffusion equation, *Journal of Geophysical Research: A*
16 tmospheres, 117, D17118, 10.1029/2012JD017618, 2012.

- 1 Bayala, M. I., and Rivas, R. E.: Enhanced sharpening procedures on edge difference and
2 water stress index basis over heterogeneous landscape of sub-humid region, *The Egyptian Journal of Remote Sensing and Space Science*, 17, 17-27, <http://dx.doi.org/10.1016/j.ejrs.2014.05.002>,
3 2014.
- 4 Bin, L., and Roni, A.: The Impact of Spatial Variability of Land-Surface Characteristics on
5 Land-Surface Heat Fluxes, *Journal of Climate*, 7, 527-537, 10.1175/1520-0442(1994)007<0527:
6 TIOSVO>2.0.CO;2, 1994.
- 7 Blyth, E. M., and Harding, R. J.: Application of aggregation models to surface heat flux from
8 the Sahelian tiger bush, *Agricultural and Forest Meteorology*, 72, 213-235, [http://dx.doi.org/10.1016/0168-1923\(94\)02164-F](http://dx.doi.org/10.1016/0168-1923(94)02164-F), 1995.
- 9 Bonan, G. B., Pollard, D., and Thompson, S. L.: Influence of Subgrid-Scale Heterogeneity
10 in Leaf Area Index, Stomatal Resistance, and Soil Moisture on Grid-Scale Land-Atmosphere Interactions, *Journal of Climate*, 6, 1882-1897, 10.1175/1520-0442(1993)006<1882:IOSSHI>2.0.CO;2, 1993.
- 11 Bonan, G. B., Levis, S., Kergoat, L., and Oleson, K. W.: Landscapes as patches of plant
12 functional types: An integrating concept for climate and ecosystem models, *Global Biogeochemical Cycles*, 16, 5-1-5-23, 10.1029/2000GB001360, 2002.
- 13 Cammalleri, C., Anderson, M. C., Gao, F., Hain, C. R., and Kustas, W. P.: A data fusion
14 approach for mapping daily evapotranspiration at field scale, *Water Resour. Res.*, 49, 4672-4686, 10.1002/wrcr.20349, 2013.
- 15 Charuchittipan, D., Babel, W., Mauder, M., Leps, J.-P., and Foken, T.: Extension of the Averaging Time in Eddy-Covariance Measurements and Its Effect on the Energy Balance Closure, *Boundary-Layer Meteorology*, 152, 303-327, 10.1007/s10546-014-9922-6, 2014.
- 16 Chen, J.: An important drawback and the improvement of the evapotranspiration model with
17 remote sensing, *Chinese Sci. Bull.*, 6, 454-457, 1988.
- 18 Chen, J., Chen, B. Z., Black, T. A., Innes, J. L., Wang, G. Y., Kiely, G., Hirano, T., and Wohlfahrt, G.: Comparison of terrestrial evapotranspiration estimates using the mass transfer and Penman-Monteith equations in land surface models, *J. Geophys. Res.-Biogeophys.*, 118, 1715-1731, 10.1002/2013jg002446, 2013.
- 19 Chen, W., Cao, C., He, Q., Guo, H., Zhang, H., Li, R., Zheng, S., Xu, M., Gao, M., Zhao, J., Li, S., Ni, X., Jia, H., Ji, W., Tian, R., Liu, C., Zhao, Y., and Li, J.: Quantitative estimation of the shrub canopy LAI from atmosphere-corrected HJ-1 CCD data in Mu Us Sandland, *Sci. China Earth Sci.*, 53, 26-33, 2010.
- 20 Choudhury, B. J., Reginato, R. J., and Idso, S. B.: An analysis of infrared temperature observations over wheat and calculation of latent heat flux, *Agr. Forest Meteorol.*, 37, 75-88, [http://dx.doi.org/10.1016/0168-1923\(86\)90029-8](http://dx.doi.org/10.1016/0168-1923(86)90029-8), 1986.
- 21 Choudhury, B. J., and Monteith, J. L.: A four-layer model for the heat budget of homogeneous land surfaces, *Q. J. Roy. Meteor. Soc.*, 114, 373-398, 10.1002/qj.49711448006, 1988.
- 22 Cleugh, H. A., Leuning, R., Mu, Q. Z., and Running, S. W.: Regional evaporation estimates from flux tower and MODIS satellite data, *Remote Sens. Environ.*, 106, 285-304, <http://dx.doi.org/10.1016/j.rse.2006.07.007>, 2007.
- 23 Colin, J., and Faivre, R.: Aerodynamic roughness length estimation from very high-resolution imaging LIDAR observations over the Heihe basin in China, *Hydrol. Earth Syst. Sci.*, 14, 2661-2669, 10.5194/hess-14-2661-2010, 2010.
- 24 Ershadi, A., McCabe, M. F., Evans, J. P., Mariethoz, G., and Kavetski, D.: A Bayesian analysis of sensible heat flux estimation: Quantifying uncertainty in meteorological forcing to improve model prediction, *Water Resources Research*, 49, 2343-2358, 10.1002/wrcr.20231, 2013a.
- 25 Ershadi, A., McCabe, M. F., Evans, J. P., and Walker, J. P.: Effects of spatial aggregation on the multi-scale estimation of evapotranspiration, *Remote Sens. Environ.*, 131, 51-62, <http://dx.doi.org/10.1016/j.rse.2012.12.007>, 2013b.
- 26 Fan, L., Xiao, Q., Wen, J., Liu, Q., Tang, Y., You, D., Wang, H., Gong, Z., and Li, X.: Evaluation of the Airborne CASI/TASI Ts-VI Space Method for Estimating Near-Surface Soil Moisture, *Remote Sensing*, 7, 3114-3137, 10.3390/rs70303114, 2015.
- 27 Fisher, J. B., Tu, K. P., and Baldocchi, D. D.: Global estimates of the land-atmosphere water flux based on monthly AVHRR and ISLSCP-II data, validated at 16 FLUXNET sites, *Remote Sens. Environ.*, 112, 901-919, <http://dx.doi.org/10.1016/j.rse.2007.06.025>, 2008.
- 28 Ha, W., Gowda, P. H., and Howell, T. A.: Downscaling of Land Surface Temperature Maps in the Texas High Plains with the TsHARP Method, *GIScience & Remote Sensing*, 48, 583-599, 10.2747/1548-1603.48.4.583, 2011.
- 29 Ha, W., Gowda, P. H., and Howell, T. A.: A review of downscaling methods for remote sensing-based irrigation management: part I, *Irrigation Science*, 31, 831-850, 10.1007/s00271-012-0331-7, 2013.
- 30 He, L., Chen, J. M., Pisek, J., Schaaf, C. B., and Strahler, A. H.: Global clumping index map derived from the MODIS BRDF product, *Remote Sens. Environ.*, 119, 118-130, <http://dx.doi.org/10.1016/j.rse.2011.12.008>, 2012.
- 31 Hu, Y., Gao, Y., Wang, J., Ji, G., Shen, Z., Cheng, L., Chen, J., and Li, S.: Some achievements in scientific research during HEIFE, *Plateau Meteorology*, 13, 225-236, 1994.
- 32 Hu, Z. L., and Islam, S.: A framework for analyzing and designing scale invariant remote

1 sensing algorithms, *Geoscience and Remote Sensing, IEEE Transactions on*, 35, 747-755, 10.11
2 09/36.581996, 1997.

3 Jia, Z. Z., Liu, S. M., Xu, Z. W., Chen, Y. J., and Zhu, M. J.: Validation of remotely se
4 nsed evapotranspiration over the Hai River Basin, China, *Journal of Geophysical Research: At
5 mospheres*, 117, D13113, 10.1029/2011JD017037, 2012.

6 Jiao, J. J., Xin, X. Z., Yu S. S., Zhou, T. and Peng, Z. Q.: Estimation of surface energy
7 balance from HJ-1 satellite data. *Journal of Remote Sensing*, 18(5), 1048-1058, doi:10.11834/jrs.
8 20143322, 2014.

9 Jiang, B., Liang, S., Townshend, J. R., and Dodson, Z. M.: Assessment of the Radiometri
10 c Performance of Chinese HJ-1 Satellite CCD Instruments, *IEEE J. Sel. Top. Appl.*, 6, 840-85
11 0, 10.1109/JSTARS.2012.2212236, 2013.

12 Jiang, L., and Islam, S.: A methodology for estimation of surface evapotranspiration over 1
13 arge areas using remote sensing observations, *Geophys. Res. Lett.*, 26, 2773-2776, 10.1029/199
14 9GL006049, 1999.

15 Jiang, L., and Islam, S.: Estimation of surface evaporation map over Southern Great Plains
16 using remote sensing data, *Water Resour. Res.*, 37, 329-340, 10.1029/2000WR900255, 2001.

17 Jiang, L., and Islam, S.: An intercomparison of regional latent heat flux estimation using r
18 emote sensing data, *Int. J. Remote Sens.*, 24, 2221-2236, 10.1080/01431160210154821, 2003.

19 Jin, Y. F., Randerson, J. T., and Goulden, M. L.: Continental-scale net radiation and evapo
20 transpiration estimated using MODIS satellite observations, *Remote Sens. Environ.*, 115, 2302-2
21 319, <http://dx.doi.org/10.1016/j.rse.2011.04.031>, 2011.

22 Kalma, J., McVicar, T., and McCabe, M.: Estimating Land Surface Evaporation: A Review
23 of Methods Using Remotely Sensed Surface Temperature Data, *Surveys in Geophysics*, 29, 42
24 1-469, 10.1007/s10712-008-9037-z, 2008.

25 Kato, S., and Yamaguchi, Y.: Analysis of urban heat-island effect using ASTER and ETM
26 + Data: Separation of anthropogenic heat discharge and natural heat radiation from sensible he
27 at flux, *Remote Sensing of Environment*, 99, 44-54, <http://dx.doi.org/10.1016/j.rse.2005.04.026>, 2
28 005.

29 Kormann, R., and Meixner, F.: An Analytical Footprint Model For Non-Neutral Stratificati
30 on, *Bound.-Lay. Meteorol.*, 99, 207-224, 10.1023/A:1018991015119, 2001.

31 Kustas, W. P.: Estimates of Evapotranspiration with a One- and Two-Layer Model of Heat
32 Transfer over Partial Canopy Cover, *J. Appl. Meteorol.*, 29, 704-715, 10.1175/1520-0450(1990)
33 029<0704:EOEWAO>2.0.CO;2, 1990.

34 Kustas, W. P., Norman, J. M., Anderson, M. C., and French, A. N.: Estimating subpixel s
35 urface temperatures and energy fluxes from the vegetation index-radiometric temperature relatio
36 nship, *Remote Sens. Environ.*, 85, 429-440, [http://dx.doi.org/10.1016/S0034-4257\(03\)00036-1](http://dx.doi.org/10.1016/S0034-4257(03)00036-1), 20
37 03.

38 Kustas, W. P., Moran, M. S., and Meyers, T. P.: The Bushland Evapotranspiration and Agr
39 icultural Remote Sensing Experiment 2008 (BEAREX08) Special Issue, *Adv. Water Resour.*, 50,
40 1-3, <http://dx.doi.org/10.1016/j.advwatres.2012.11.006>, 2012.

41 Leuning, R., Zhang, Y. Q., Rajaud, A., Cleugh, H., and Tu, K.: A simple surface conduct
42 ance model to estimate regional evaporation using MODIS leaf area index and the Penman-Mo
43 nteith equation, *Water Resour. Res.*, 44, W10419, 10.1029/2007WR006562, 2008.

44 Li, H., Liu, Q. H., Zhong, B., Du, Y. M., Wang, H. S., and Wang, Q.: A single-channel
45 algorithm for land surface temperature retrieval from HJ-1B/IRS data based on a parametric m
46 odel, *Geoscience and Remote Sensing Symposium (IGARSS)*, 2010 IEEE International, Honolul
47 u, Hawaii, USA, 2448-2451, 2010a.

48 Li, H., Liu, Q., Jiang, J., Wang, H., and Sun, L.: Validation of the land surface temperatu
49 re derived from HJ-1B/IRS data with ground measurements, *Geoscience and Remote Sensing S
50 yposium (IGARSS)*, 2011 IEEE International, Vancouver, Canada, 293-296, 2011a.

51 Li, H., Sun, D., Yu, Y., Wang, H., Liu, Y., Liu, Q., Du, Y., Wang, H., and Cao, B.: Eval
52 uation of the VIIRS and MODIS LST products in an arid area of Northwest China, *Remote S
53 ens. Environ.*, 142, 111-121, <http://dx.doi.org/10.1016/j.rse.2013.11.014>, 2014.

54 Li, J., Gu, X., Li, X., Yu, T., Chen, H., and Long, M.: Validation of HJ-1B Thermal Ban
55 d On-board Calibration and Its Sensitivity Analysis, *Remote Sensing Information*, 1, 3-9, doi:10
56 .3969/j.issn.1000-3177.2011.01.001, 2011b.

57 Li, L., Xin, X. Z., Su, G. L., and Liu, Q. H.: Photosynthetically active radiation retrieval
58 based on HJ-1A/B satellite data, *Sci. China Earth Sci.*, 53, 81-91, 10.1007/s11430-010-4142-5,
59 2010b.

60 Li, X., Li, X. W., Li, Z. Y., Ma, M. G., Wang, J., Xiao, Q., Liu, Q., Che, T., Chen, E.
61 X., Yan, G. J., Hu, Z. Y., Zhang, L. X., Chu, R. Z., Su, P. X., Liu, Q. H., Liu, S. M., Wang
62 , J. D., Niu, Z., Chen, Y., Jin, R., Wang, W. Z., Ran, Y. H., Xin, X. Z., and Ren, H. Z.: Wa
63 tershed Allied Telemetry Experimental Research, *Journal of Geophysical Research: Atmospheres*,
64 114, D22103, 10.1029/2008JD011590, 2009.

65 Li, X., Cheng, G. D., Liu, S. M., Xiao, Q., Ma, M. G., Jin, R., Che, T., Liu, Q. H., Wa
66 ng, W. Z., Qi, Y., Wen, J. G., Li, H. Y., Zhu, G. F., Guo, J. W., Ran, Y. H., Wang, S. G., Z
67 hu, Z. L., Zhou, J., Hu, X. L., and Xu, Z. W.: Heihe Watershed Allied Telemetry Experimenta
68 l Research (HiWATER): Scientific Objectives and Experimental Design, *B. Am. Meteorol. Soc.*,
69 94, 1145-1160, 10.1175/BAMS-D-12-00154.1, 2013a.

1 Li, Z. L., Tang, B. H., Wu, H., Ren, H., Yan, G., Wan, Z., Trigo, I. F., and Sobrino, J.
2 A.: Satellite-derived land surface temperature: Current status and perspectives, *Remote Sensing*
3 of Environment, 131, 14-37, <http://dx.doi.org/10.1016/j.rse.2012.12.008>, 2013b.

4 Liang, S., Stroeve, J., and Box, J. E.: Mapping daily snow/ice shortwave broadband albed
5 o from Moderate Resolution Imaging Spectroradiometer (MODIS): The improved direct retrieval
6 algorithm and validation with Greenland *in situ* measurement, *Journal of Geophysical Research*
7 : Atmospheres, 110, D10109, [10.1029/2004JD005493](https://doi.org/10.1029/2004JD005493), 2005.

8 Liang, S. L., Zhang, X. T., Xiao, Z. Q., Cheng, J., Liu, Q., and Zhao, X.: Global Land
9 Surface Satellite (GLASS) Products: Algorithms, Validation and Analysis, 1 ed., SpringerBriefs
10 in Earth Sciences, Springer International Publishing, 2014.

11 Liu, Q., Qu, Y., Wang, L. Z., Liu, N. F., and Liang, S. L.: Glass-Global Land Surface Br
12 oadband Albedo Product: Algorithm Theoretical Basis Document. Version, 1, 1-50, College of
13 Global Change and Earth System Science, Beijing Normal University, 2011a.

14 Liu, S. M., Xu, Z. W., Wang, W. Z., Jia, Z. Z., Zhu, M. J., Bai, J., and Wang, J. M.: A
15 comparison of eddy-covariance and large aperture scintillometer measurements with respect to t
16 he energy balance closure problem, *Hydrol. Earth Syst. Sci.*, 15, 1291-1306, 2011b.

17 Liu, S., Xu, Z., Song, L., Zhao, Q., Ge, Y., Xu, T., Ma, Y., Zhu, Z., Jia, Z., and Zhang,
18 F.: Upscaling evapotranspiration measurements from multi-site to the satellite pixel scale over h
19 eterogeneous land surfaces, *Agricultural and Forest Meteorology*, <http://dx.doi.org/10.1016/j.agrfor>
20 [met.2016.04.008](https://doi.org/10.1016/j.agrfor.2016.04.008), 2016.

21 Long, D., and Singh, V. P.: A modified surface energy balance algorithm for land (M-SEB
22 AL) based on a trapezoidal framework, *Water Resour. Res.*, 48, W02528, [10.1029/2011WR0106](https://doi.org/10.1029/2011WR0106)
23 [07](https://doi.org/10.1029/2011WR010607), 2012a.

24 Long, D., and Singh, V. P.: A Two-source Trapezoid Model for Evapotranspiration (TTME)
25 from satellite imagery, *Remote Sens. Environ.*, 121, 370-388, <http://dx.doi.org/10.1016/j.rse.201>
26 [2.02.015](https://doi.org/10.1016/j.rse.2012.02.015), 2012b.

27 Maayar, E. M., and Chen, J. M.: Spatial scaling of evapotranspiration as affected by heter
28 ogeneities in vegetation, topography, and soil texture, *Remote Sens. Environ.*, 102, 33-51, [http://](http://dx.doi.org/10.1016/j.rse.2006.01.017)
29 [dx.doi.org/10.1016/j.rse.2006.01.017](https://doi.org/10.1016/j.rse.2006.01.017), 2006.

30 Mallick, K., Boegh, E., Trebs, I., Alfieri, J. G., Kustas, W. P., Prueger, J. H., Niyogi, D.,
31 Das, N., Drewry, D. T., Hoffmann, L., and Jarvis, A. J.: Reintroducing radiometric surface tem
32 perature into the Penman-Monteith formulation, *Water Resources Research*, 51, 6214-6243, [10.1](https://doi.org/10.1029/2014WR016106)
33 [002/2014WR016106](https://doi.org/10.1029/2014WR016106), 2015.

34 McCabe, M. F., and Wood, E. F.: Scale influences on the remote estimation of evapotrans
35 piration using multiple satellite sensors, *Remote Sensing of Environment*, 105, 271-285, [10.101](https://doi.org/10.1016/j.rse.2006.07.006)
36 [6/j.rse.2006.07.006](https://doi.org/10.1016/j.rse.2006.07.006), 2006.

37 Meyers, T. P., and Hollinger, S. E.: An assessment of storage terms in the surface energy
38 balance of maize and soybean, *Agricultural and Forest Meteorology*, 125, 105-115, [http://dx.doi.](http://dx.doi.org/10.1016/j.agrformet.2004.03.001)
39 [org/10.1016/j.agrformet.2004.03.001](https://doi.org/10.1016/j.agrformet.2004.03.001), 2004.

40 Moran, M. S., Humes, K. S., and Pinter Jr, P. J.: The scaling characteristics of remotely-s
41 ensed variables for sparsely-vegetated heterogeneous landscapes, *Journal of Hydrology*, 190, 337
42 -362, [http://dx.doi.org/10.1016/S0022-1694\(96\)03133-2](http://dx.doi.org/10.1016/S0022-1694(96)03133-2), 1997.

43 Mu, Q. Z., Zhao, M. S., and Running, S. W.: Improvements to a MODIS global terrestria
44 l evapotranspiration algorithm, *Remote Sens. Environ.*, 115, 1781-1800, [http://dx.doi.org/10.1016/](http://dx.doi.org/10.1016/j.rse.2011.02.019)
45 [j.rse.2011.02.019](https://doi.org/10.1016/j.rse.2011.02.019), 2011.

46 Mukherjee, S., Joshi, P. K., and Garg, R. D.: A comparison of different regression models
47 for downscaling Landsat and MODIS land surface temperature images over heterogeneous lan
48 dscape, *Advances in Space Research*, 54, 655-669, <http://dx.doi.org/10.1016/j.asr.2014.04.013>, 20
49 14.

50 Neftel, A., Spirig, C., and Ammann, C.: Application and test of a simple tool for operatio
51 nal footprint evaluations, *Environ. Pollut.*, 152, 644-652, <http://dx.doi.org/10.1016/j.envpol.2007.0>
52 [6.062](https://doi.org/10.1016/j.envpol.2007.06.062), 2008.

53 Nilson, T.: A theoretical analysis of the frequency of gaps in plant stands, *Agr. Meteorol.*
54 8, 25-38, 1971.

55 Norman, J. M., Kustas, W. P., and Humes, K. S.: Source approach for estimating soil and
56 vegetation energy fluxes in observations of directional radiometric surface temperature, *Agr. F*
57 *orest Meteorol.*, 77, 263-293, [http://dx.doi.org/10.1016/0168-1923\(95\)02265-Y](http://dx.doi.org/10.1016/0168-1923(95)02265-Y), 1995.

58 Norman, J. M., Anderson, M. C., Kustas, W. P., French, A. N., Mecikalski, J., Torn, R.,
59 Diak, G. R., Schmugge, T. J., and Tanner, B. C. W.: Remote sensing of surface energy fluxes
60 at 101-m pixel resolutions, *Water Resour. Res.*, 39, 1221, [10.1029/2002WR001775](https://doi.org/10.1029/2002WR001775), 2003.

61 Paulson, C. A.: The mathematical representation of wind speed and temperature profiles in
62 the unstable atmospheric surface layer, *J. Appl. Meteorol.*, 9, 857-861, 1970.

63 Prueger, J. H., Hatfield, J. L., Parkin, T. B., Kustas, W. P., Hipps, L. E., Neale, C. M. U.
64 , MacPherson, J. I., Eichinger, W. E., and Cooper, D. I.: Tower and Aircraft Eddy Covariance
65 Measurements of Water Vapor, Energy, and Carbon Dioxide Fluxes during SMACEX, *Journal o*
66 [f Hydrometeorology](https://doi.org/10.1175/JHM457.1), 6, 954-960, [10.1175/JHM457.1](https://doi.org/10.1175/JHM457.1), 2005.

67 Shuttleworth, W. J., and Wallace, J.: Evaporation from sparse crops - an energy combinatio
68 n theory, *Q. J. Roy. Meteor. Soc.*, 111, 839-855, 1985.

69 Song, Y., Wang, J. M., Yang, K., Ma, M. G., Li, X., Zhang, Z. H., and Wang, X. F.: A

1 revised surface resistance parameterisation for estimating latent heat flux from remotely sensed
2 data, *Int. J. Appl. Earth Obs.*, 17, 76-84, <http://dx.doi.org/10.1016/j.jag.2011.10.011>, 2012.

3 Su, Z.: The Surface Energy Balance System (SEBS) for estimation of turbulent heat fluxes
4 , *Hydrol. Earth Syst. Sci.*, 6, 85-100, 10.5194/hess-6-85-2002, 2002.

5 Sun, L., Sun, R., Li, X. W., Chen, H. L., and Zhang, X. F.: Estimating Evapotranspiration
6 using Improved Fractional Vegetation Cover and Land Surface Temperature Space, *Journal of*
7 *Resources and Ecology*, 2, 225-231, 10.3969/j.issn.1674-764x.2011.03.005, 2011.

8 Sun, L., Liang, S. L., Yuan, W. P., and Chen, Z. X.: Improving a Penman–Monteith evap
9 otranspiration model by incorporating soil moisture control on soil evaporation in semiarid area
10 s, *International Journal of Digital Earth*, 6, 134-156, 10.1080/17538947.2013.783635, 2013.

11 Valor, E., and Caselles, V.: Mapping land surface emissivity from NDVI: Application to E
12 uropean, African, and South American areas, *Remote Sens. Environ.*, 57, 167-184, [http://dx.doi.org/10.1016/0034-4257\(96\)00039-9](http://dx.doi.org/10.1016/0034-4257(96)00039-9), 1996.

13 Venturini, V., Islam, S., and Rodriguez, L.: Estimation of evaporative fraction and evapotra
14 nspiration from MODIS products using a complementary based model, *Remote Sens. Environ.*,
15 112, 132-141, <http://dx.doi.org/10.1016/j.rse.2007.04.014>, 2008.

16 Vermote E F, Tanre D, Deuze J L, et al. Second Simulation of a Satellite Signal in the S
17 olar Spectrum-Vector. 6S User Guide Version 3, 2006.

18 Von Randow, C., Kruijt, B., Holtslag, A. A. M., and de Oliveira, M. B. L.: Exploring ed
19 dy-covariance and large-aperture scintillometer measurements in an Amazonian rain forest, *Agric
20 cultural and Forest Meteorology*, 148, 680-690, <http://dx.doi.org/10.1016/j.agrformet.2007.11.011>,
21 2008.

22 Wang, K. C., and Liang, S. L.: An improved method for estimating global evapotranspirati
23 on based on satellite determination of surface net radiation, vegetation index, temperature, and
24 soil moisture, *Geoscience and Remote Sensing Symposium*, 2008. IGARSS 2008. IEEE Internat
25 ional, Boston, Massachusetts, USA, III - 875-III - 878, 2008.

26 Wang, Q., Wu, C., Li, Q., and Li, J.: Chinese HJ-1A/B satellites and data characteristics,
27 *Sci. China Earth Sci.*, 53, 51-57, 10.1007/s11430-010-4139-0, 2010.

28 Xin, X., and Liu, Q.: The Two-layer Surface Energy Balance Parameterization Scheme (T
29 SEBPS) for estimation of land surface heat fluxes, *Hydrol. Earth Syst. Sci.*, 14, 491-504, 10.51
30 94/hess-14-491-2010, 2010.

31 Xin, X., Liu, Y. N., Liu, Q., and Tang, Y.: Spatial-scale error correction methods for regi
32 onal fluxes retrieval using MODIS data, *J. Remote Sens.*, 16(2), 207-231, 2012.

33 Xu, T. R., Bateni, S. M., and Liang, S. L.: Estimating Turbulent Heat Fluxes With a Wea
34 k-Constraint Data Assimilation Scheme: A Case Study (HiWATER-MUSOEXE), *IEEE Geosci.
35 Remote S.*, 12, 68-72, 10.1109/LGRS.2014.2326180, 2015.

36 Xu, Z. W., Liu, S. M., Li, X., Shi, S. J., Wang, J. M., Zhu, Z. L., Xu, T. R., Wang, W.
37 Z., and Ma, M. G.: Intercomparison of surface energy flux measurement systems used during t
38 he HiWATER - MUSOEXE, *Journal of Geophysical Research: Atmospheres*, 118, 13,140-113,15
39 7, 10.1002/2013JD020260, 2013.

40 Yang, K., and Wang, J.: A temperature prediction-correction method for estimating surface
41 soil heat flux from soil temperature and moisture data, *Sci. China Ser. D-Earth Sci.*, 51, 721-7
42 29, 10.1007/s11430-008-0036-1, 2008.

43 Yang, Y. T., and Shang, S. H.: A hybrid dual-source scheme and trapezoid framework-bas
44 ed evapotranspiration model (HTEM) using satellite images: Algorithm and model test, *Journal
45 of Geophysical Research: Atmospheres*, 118, 2284-2300, 10.1002/jgrd.50259, 2013.

46 Yao, Y. J., Liang, S. L., Cheng, J., Liu, S. M., Fisher, J. B., Zhang, X. D., Jia, K., Zhao,
47 X., Qin, Q. M., Zhao, B., Han, S., Jie, Zhou, G. S., Zhou, G. Y., Li, Y. L., and Zhao, S. H.
48 : MODIS-driven estimation of terrestrial latent heat flux in China based on a modified Priestle
49 y–Taylor algorithm, *Agr. Forest Meteorol.*, 171–172, 187-202, <http://dx.doi.org/10.1016/j.agrforme>
50 t.2012.11.016, 2013.

51 Yebra, M., Van Dijk, A., Leuning, R., Huete, A., and Guerschman, J. P.: Evaluation of op
52 tical remote sensing to estimate actual evapotranspiration and canopy conductance, *Remote Sens
53 . Environ.*, 129, 250-261, <http://dx.doi.org/10.1016/j.rse.2012.11.004>, 2013.

54 Yu, S., Xin, X., and Liu, Q.: Estimation of clear-sky longwave downward radiation from
55 HJ-1B thermal data, *Sci. China Earth Sci.*, 56, 829-842, 10.1007/s11430-012-4507-z, 2013.

56 Zhang, R., Sun, X., Wang, W., Xu, J., Zhu, Z., and Tian, J.: An operational two-layer re
57 mote sensing model to estimate surface flux in regional scale: physical background, *Sci. China
58 Ser. D*, 34, 200-216, 2005.

59 Zhang, X., Zhao, X., Liu, G., Kang, Q., and Wu, D.: Radioactive Quality Evaluation and
60 Cross Validation of Data from the HJ-1A/B Satellites' CCD Sensors, *Sensors*, 13, 8564, doi:10.
61 3390/s130708564, 2013.

62 Zhong, B., Ma, P., Nie, A., Yang, A., Yao, Y., Lü W., Zhang, H., and Liu, Q.: Land cov
63 er mapping using time series HJ-1/CCD data, *Sci. China Earth Sci.*, 57, 1790-1799, 10.1007/s1
64 1430-014-4877-5, 2014a.

65 Zhong, B., Zhang, Y., Du, T., Yang, A., Lv, W., and Liu, Q.: Cross-Calibration of HJ-1/C
66 CD Over a Desert Site Using Landsat ETM+ Imagery and ASTER GDEM Product, *Geoscienc
67 e and Remote Sensing*, *IEEE Transactions on*, 52, 7247-7263, 10.1109/TGRS.2014.2310233, 20
68 14b.

1 Zhu, G. F., Su, Y. H., Li, X., Zhang, K., and Li, C. B.: Estimating actual evapotranspirati
2 on from an alpine grassland on Qinghai-Tibetan plateau using a two-source model and paramet
3 er uncertainty analysis by Bayesian approach, *J. Hydrol.*, 476, 42-51, 10.1016/j.jhydrol.2012.10.
4 006, 2013.